Received: 7 September 2025 | Revised: 2 February 2026 | Accepted: 26 February 2026

DOI: 10.1002/dep2.70070

The Depositional Record Open Access
A journal of the International Association of Sedimentologists
IAS WILEY

ORIGINAL ARTICLE

Supercritical-flow structures in a Cretaceous submarine channel–lobe transition zone, Point Loma Formation, California

Luthfi Saifudin | **Zane Jobe** | **Arnoud Slootman** | **Mary Carr** | **Piret Plink-Björklund**

Department of Geology and Geological Engineering, Colorado School of Mines, Golden, Colorado, USA

Correspondence
Zane Jobe, Department of Geology and Geological Engineering, Colorado School of Mines, Golden, CO, USA.
Email: zanejobe@gmail.com

Funding information
Lembaga Pengelola Dana Pendidikan; Indonesian Endowment of Education (LPDP); International Association of Sedimentologists (IAS) Judith McKenzie Award; Bartshe Fund at Colorado School of Mines; Lee Billingsley Graduate Fellowship at Colorado School of Mines; Society for Sedimentary Geology (SEPM)

Abstract

Submarine fan deposits are important archives of Earth's history and serve as the record of turbidity current events that transfer large amounts of terrestrial sediment and carbon into the ocean. The geomorphology, depositional processes and facies architecture change significantly along the submarine-fan depositional profile, particularly at the channel–lobe transition zone (CLTZ). However, few studies have documented detailed facies architecture and associated sedimentary structures in the CLTZ, which are important for paleoenvironmental interpretations and morphometric information essential to reconstructing sediment transport dynamics and reservoir connectivity in ancient successions. Excellent coastal-cliff outcrops from ancient CLTZ deposits of the Upper Cretaceous Point Loma Formation in San Diego, California constrain the facies architecture of the CLTZ and the three-dimensional geometry of supercritical-flow bedforms. We update previous work on sand-rich and mud-rich lobe complexes at Sunset Cliffs and present the first description of the uppermost sand-rich CLTZ complex that contains antidune deposits arranged in predominantly metre-thick tabular packages. Paleocurrent data suggest a compensatory evolution between elements and complexes that was probably driven by updip avulsions. The data generated by this study help to characterise the detailed facies architecture and bedform geometry for CLTZ deposits, which enables a better understanding of the sediment transport dynamics of the channel–lobe transition zone. These data, when combined with other ancient and modern analogues, can be used to predict reservoir connectivity and heterogeneity in CLTZ deposits that form hydrocarbon reservoirs and potential carbon storage sites.

KEYWORDS

antidunes, channel-lobetransition zone, froude supercriticalflow, point loma formation, San Diego, California, submarine fan

1 | INTRODUCTION

Submarine channel-fan systems are an important element in sediment routing systems for transferring terrestrial sediment (Hessler & Fildani, 2019; Talling et al., 2022), organic carbon (Hage et al., 2020; Talling et al., 2024) and microplastics (Kane & Clare, 2019) to the deep ocean sink. The channel–lobe transition zone (CLTZ) separates channelised slope systems from unconfined lobate systems (Brooks et al., 2018, 2022; Carr & Gardner, 2000; Kenyon et al., 1995; Mutti & Normark, 1987; Normark et al., 1979; Pemberton et al., 2016; Wynn et al., 2002). The presence or absence of a CLTZ has important implications for subsurface reservoir–fluid connectivity between sandy channel-fill and lobe facies (Wynn et al., 2002). Simple models for CLTZ deposits (Normark et al., 1979) have been shown to be much more complex with recent modern-seafloor surveys (Carvajal et al., 2017; Droz et al., 2020; Englert et al., 2021; Wynn et al., 2002), outcrop observations (Brooks et al., 2022; Hofstra et al., 2015; Ito, 2008; Mansor & Amir Hassan, 2021; Pemberton et al., 2016) and experimental studies (Cantelli et al., 2011; Cantero et al., 2014; Wilkin et al., 2023) that document CLTZ geomorphology, flow dynamics and preserved depositional architecture. The CLTZ is characterised geomorphologically by a rapid decrease in longitudinal slope that affects turbidity-current dynamics and a loss of lateral confinement (Mutti & Normark, 1987). Commonly, turbidity currents are Froude-supercritical in canyon-channel reaches (Cantelli et al., 2011; Lang, Sievers, et al., 2017; Sequeiros, 2012) and react to a decrease in confinement and longitudinal gradient at the CLTZ with a series of hydraulic jumps that promote erosion and deposition (Pohl et al., 2020). Both erosional features (including isolated and amalgamated scours, cyclic steps and erosional lineations) and depositional features (including amalgamated sand bodies, antidunes, sediment waves, sediment mounds/bars at scour mouths, scour-and-fill structures and thin, patchy sand and gravel accumulations) characterise CLTZ deposits (Carvajal et al., 2017; Cornard et al., 2025; Cornard & Pickering, 2020; Droz et al., 2020; Hofstra et al., 2018; Lobato et al., 2025; Pemberton et al., 2016; Wynn et al., 2002). The largest isolated scours occur in the proximal CLTZ, and smaller isolated scours and sediment waves tend to occur farther basinward (Hofstra et al., 2018; Jobe et al., 2012; Lobato et al., 2025; Wynn et al., 2002).

Ancient CLTZ deposits are limited because of the difficulties in placing an outcrop into its larger-scale depositional context as well as recognising large-scale scours and coarse-grained bedforms in outcrop. Thus, most CLTZ deposits described in outcrop are from well-constrained systems (e.g. Karoo Basin in South Africa, Tres Pasos Formation in Chile) and are typified by paleocurrent variability, complex alternation of erosional and depositional architecture and composite erosional surfaces, abundant erosional scours of various scales and localised lenses of mudclasts and coarse-grained sediment (Brooks et al., 2018, 2022; Cornard et al., 2025; Hofstra et al., 2015, 2018; Pemberton et al., 2016; Pohl et al., 2022).

This study characterises the facies architecture of CLTZ deposits in excellent seacliff exposures of the Upper Cretaceous Point Loma Formation in San Diego, California. Using three-dimensional (3D) digital outcrop models, measured sections and paleocurrent measurements, we document a previously undescribed lobe complex in the uppermost Point Loma Formation and characterise the stratigraphic architecture and bed-scale sedimentary structures to reconstruct the formative sediment gravity-flow processes that shape the CLTZ. Data from this study can be used to better parameterise reservoir models for subsurface CLTZ deposits that form hydrocarbon reservoirs, carbon-sequestration and cyclic hydrogen-storage sites.

2 | LOBE-DEPOSIT HIERARCHY

Lobe hierarchy describes the typical compensational stacking patterns of submarine lobe deposits and is useful for comparing facies and architectural variability at multiple scales. Several classification schemes exist for lobe deposits (Cullis et al., 2018; Deptuck et al., 2008; Mutti & Normark, 1987; Prélat et al., 2009), with the hierarchy generally consisting of three or four levels: the event bed, the lobe element, the composite 'lobe' (which is omitted in some classifications) and the lobe complex. The smallest unit is the event bed, comprised of the stacked lithological units derived from a single sediment-gravity-flow 'event' (e.g. a turbidity current). Over time, two or more event beds stack to form a lobe element; a subsequent lobe element is formed when avulsion of an up-dip feeder redirects sediment deposition to a new location. In the four-level hierarchy, multiple lobe elements form a 'composite lobe' (Deptuck et al., 2008) or 'lobe' (Prélat et al., 2009), and multiple 'lobes' form lobe complexes. In the three-level hierarchy, the lobe is omitted, and lobe elements stack to form lobe complexes (e.g. Pyles et al., 2019). Some studies also include a larger hierarchical level that is termed 'lobe complex set' or 'lobe system' or 'fan', which is roughly equivalent to the largest-scale compensation happening on a submarine fan (e.g. Picot et al., 2016).

This study will follow the three-level hierarchy of Pyles et al. (2019), where beds stack to form lobe elements, and lobe elements stack to form lobe complexes, while recognising that this scheme does not include the 'lobe' level that is common in other schemes (e.g. Cullis et al., 2018). We will

not speculate as to the largest-scale organisation of the depositional 'system' due to the disparity in the dimensions of the study area outcrops in comparison to well-mapped lobe-deposit dimensions. For example, typical lobe elements have lengths and widths in the 1000s to 10,000s of metres and thicknesses of 1–10 m (Pettinga et al., 2018). Due to the size of the study area (*ca* 2 km wide, but with stratal dips that allow only a window of *ca* 400 m for any single element) and the orientation of the outcrop oblique to paleoflow direction, it is very unlikely that a full element is visible. Lastly, Pyles et al. (2019) also use two other hierarchical terms that will also be used in this study: (1) 'mudstone sheets' that are either the lateral or distal equivalent to a lobe complex/lobe system or represent a system-wide shutdown of sediment supply; similar muddy units are defined as 'interlobe' units by Prélat et al. (2009); and (2) 'mass-transport complexes' (MTCs) that are composed of multiple 'mass-transport elements' that likely represent individual mass-transport-deposits (i.e. individual events, also see discussion in Simabrata et al., 2025). While the hierarchical grouping of mass-transport deposits is not common, it serves to maintain consistent nomenclature for the groupings of stratigraphic packages.

3 | GEOLOGICAL BACKGROUND

The Upper Cretaceous Rosario Group that crops out in the San Diego coastal area (Figure 1) comprises *ca* 500 m of stratigraphy, including non-marine conglomerate at the base (Lusardi Formation), submarine-lobe deposits (Point Loma Formation) and submarine-channel deposits (Cabrillo Formation) at the top (Kennedy & Moore, 1971). The Rosario Group sediments were deposited in the Peninsular Ranges forearc basin and likely sourced from the Peninsular Ranges Batholith (Sharman et al., 2015). The northern Peninsular Ranges Batholith in southern California is one segment of the Cordilleran Arc that developed on the western margin of North America during the eastward subduction of the Farallon oceanic plate (Figure 1C; Jiang & Lee, 2017). The Lusardi Formation is interpreted to represent deposits from alluvial fans (Kennedy & Moore, 1971), and consists of cobble to boulder conglomerate, with interbedded lenses of sandstone. The Lusardi Formation has a basal contact with batholithic and pre-batholithic rocks (Peterson & Nordstorm, 1970) and its upper contact is seemingly conformable with the Point Loma Formation. The Point Loma Formation is composed of deep-marine sandstones and

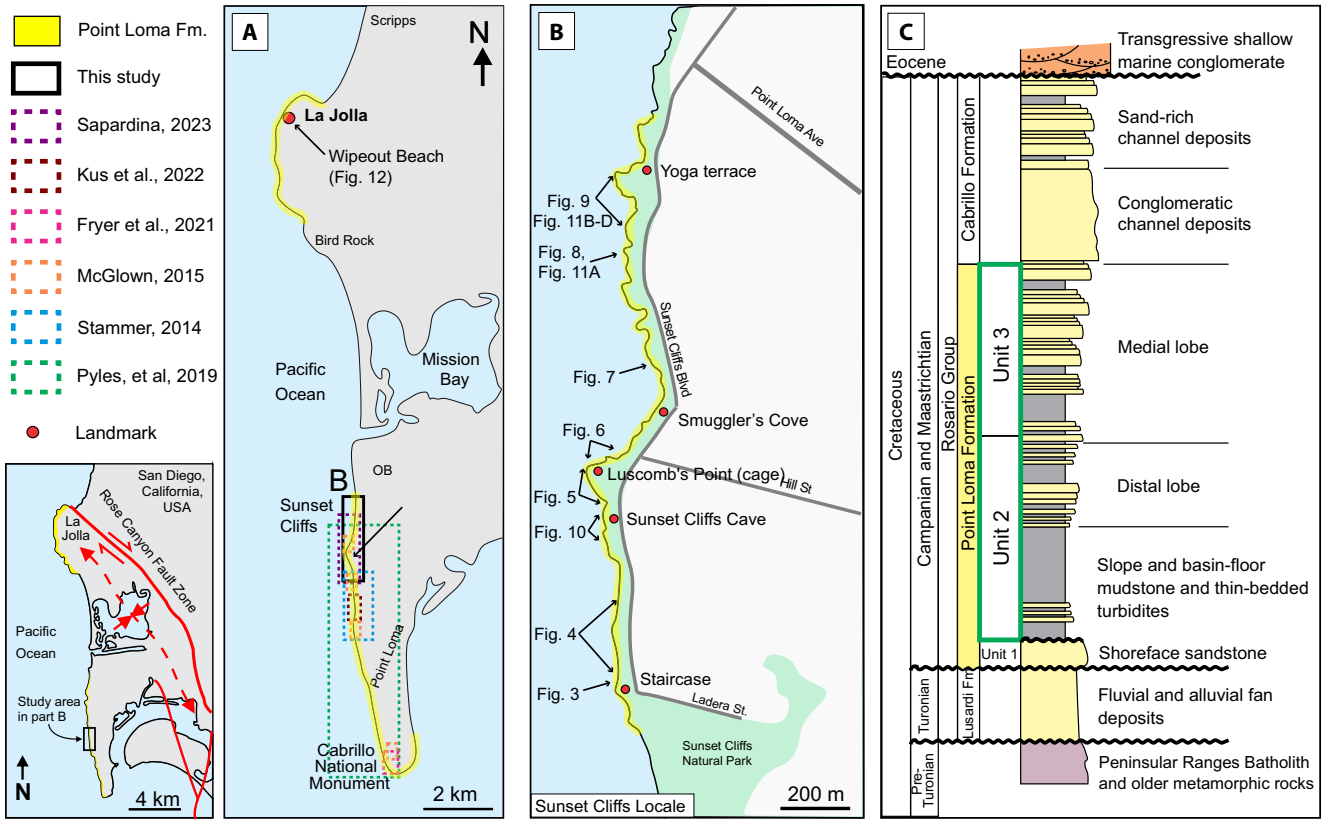

FIGURE 1 Study area for the Point Loma Formation (modified from Kus et al., 2022). (A) San Diego coastline with Point Loma Formation outcrops at La Jolla and Sunset Cliffs. (B) Sunset Cliffs locale with figure locations, and notable streets and landmarks indicated. (C) Stratigraphic column for Cretaceous sedimentary rocks near San Diego (stacking patterns are schematised; modified from Nilsen & Abbott, 1981).

mudstones deposited in water depths in excess of 700 m (Sliter, 1984) and crops out along the seacliffs on the west side of the Point Loma Peninsula and also along La Jolla Bay (Figure 1A,B). The Point Loma Formation is interpreted to represent submarine lobe deposits (Fryer et al., 2021; Kus et al., 2022; Nilsen & Abbott, 1981; Pyles et al., 2019). The contact between the Point Loma and Cabrillo formations is gradational and interpreted to represent progradation of a submarine-fan system (Figure 1C). The Cabrillo Formation consists of sandstones and conglomerates (Nilsen & Abbott, 1981) that likely represent conglomeratic submarine-channel deposits (cf. Hickson & Lowe, 2002; Jaikla, 2021; Jobe et al., 2010). An angular unconformity separates the Point Loma Formation in the study area with overlying Pleistocene alluvial sediments mapped regionally as the Bay Point Formation and the Linda Vista Formation (Kennedy, 1975); in subsequent figures, we refer to these deposits as undifferentiated Pleistocene sediments as to not infer specificity.

This study focuses on the upper portion of the Point Loma Formation, exposed at two localities: along Sunset Cliffs on the northern Point Loma Peninsula and just south of La Jolla Bay (Figure 1A). A broad syncline at Mission Bay separates these two areas, and the exact age correlation between strata exposed on the Point Loma Peninsula and strata exposed at La Jolla Bay is unclear. Near La Jolla Bay, the Point Loma Formation is transected by the Rose Canyon Fault Zone, a Neogene dextral strike-slip fault with unknown displacement (Girty, 1987) that juxtaposes Cretaceous strata (southwest) and Eocene strata (northeast) (Kennedy & Moore, 1971; Peterson & Nordstorm, 1970).

3.1 | Point Loma Formation

In the La Jolla area, no modern work has been completed in the Point Loma Formation since the work of Nilsen and Abbott (1981). However, on the Point Loma Peninsula, the Point Loma Formation has been well studied in the last decade, focusing on the overall stacking patterns and lateral heterogeneity (Fleming, 2010; Fryer et al., 2021; Kus et al., 2022; McGlown, 2015; Pyles et al., 2019; Sapardina, 2023; Stammer, 2014). The lobe deposits of the Point Loma Formation include mass-transport deposits, debrites, turbidites and occasional hybrid event beds (HEBs, sensu Haughton et al., 2009) ranging from <10 cm up to 5 m in bed thickness (Pyles et al., 2019). The Point Loma Formation was previously divided into three units by Yeo (1984) (Figure 1C): Unit 1, a lower sandstone unit interpreted to represent an inner-shelf-to-shoreface environment; Unit 2, a middle mudstone unit with thin-bedded sandstone interpreted to represent distal submarine-fan deposits; and Unit 3, an upper interbedded mudstone and thick-bedded sandstone unit that is interpreted to represent a medial submarine-fan environment. More recent work has focussed on the combined Units 2 and 3, with modern nomenclature that supersedes these 'units': four lobe complexes composed of 27 lobe elements and one mass-transport-complex composed of four mass-transport elements described from seacliff exposures on the Point Loma Peninsula (Fleming, 2010; Pyles et al., 2019).

Several other studies have answered more specific questions about lobe architecture and depositional processes in the Point Loma Formation. McGlown (2015) focussed on turbidite and HEB depositional processes and lateral continuity in Lobe Complex 1, whereas Stammer (2014) studied an axis-to-fringe transect of a lobe element in Lobe Complex 2, documenting fringe-ward increases in mud content, organic matter and mineralogical fractionation, with less quartz and more K-feldspar, plagioclase and biotite towards the fringe. Kus et al. (2022) and Fryer et al. (2021) studied the lateral heterogeneity of event beds and lobe elements within Lobe Complexes 1 and 3, respectively. These bed-scale studies represent a step forward in understanding subenvironments within lobe deposits by comparison to a large database collected by Fryer and Jobe (2019). Most recently, Sapardina (2023) proposed that the formation of the Point Loma submarine fan occurred through channel avulsions rather than bifurcations into distributary channels.

This study focuses on the Sunset Cliffs locale (Figure 1B) on the Point Loma Peninsula that beautifully exposes a variety of sediment-gravity-flow deposits in Complexes 4 to 6 (Figure 2) that are interpreted here as an outcrop analogue for CLTZ deposits. We also document similar facies from the La Jolla locale (Figure 1A), and the synthesis of these two locales better constrains the facies architecture, bedform morphology and erosional-scour dimensions of CLTZ deposits in the uppermost Point Loma Formation.

4 | DATA AND METHODOLOGY

Digital outcrop models for the Sunset Cliffs and La Jolla locales of the Point Loma Formation were built using photographs collected from DJI Phantom 4 Pro and Mavic 3 Pro drones and processed using Agisoft Metashape to construct a textured 3D mesh (Figure 2A). The two outcrop models are approximately 12 m tall, and 2 km long in Sunset Cliffs and 1.6 km long in La Jolla. The stratigraphic architecture and structural discontinuities were interpreted in Virtual Reality Geological Studio (VRGS, a software package created by VRGeoscience Limited) using principles of allostratigraphy and mappable lateral

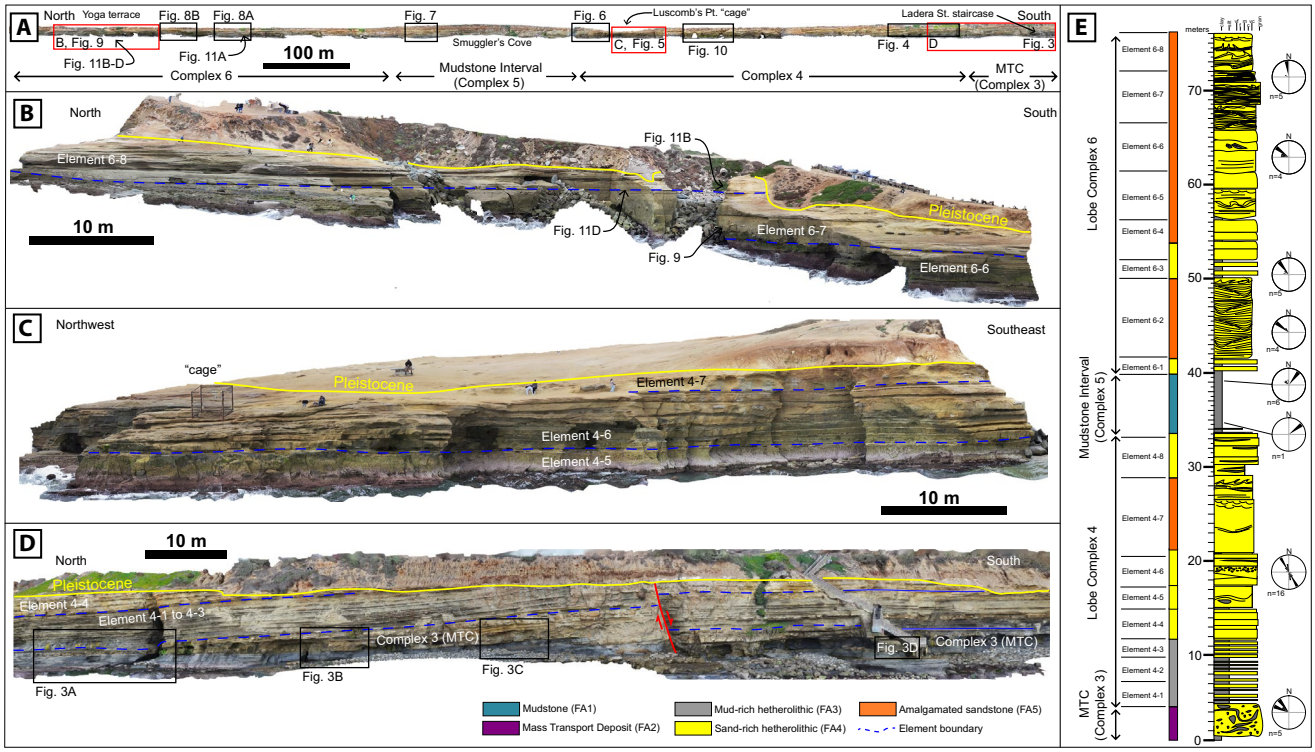

FIGURE 2 Point Loma channel–lobe transition zone (CLTZ) deposits at Sunset Cliffs. (A) Digital outcrop model overview. Red boxes show locations of parts (B, C and D) of this figure, and black boxes and arrows show locations of other figures. (B) Thick amalgamated, antidune-rich sandstone of Complex 6. (C) Bedded sandstone with erosional features (interpreted as cyclic steps) of upper Complex 4. (D) Thin-bedded mudstones–sandstones of Complex 4 overlying mass-transport deposits of Complex 3. (E) Composite graphic log showing the overall stacking and evolution of the Point Loma CLTZ deposits.

changes in lithology and facies. Stratigraphic relationships are displayed on orthomosaic photo panels (e.g. Figure 2A) derived from digital outcrop models. The outcrops were logged in the field to record bed thickness, grain size (following the methods of Jobe et al., 2021), sedimentary structures, and paleocurrent directions. The outcrop model was also used to extract digital graphic logs from inaccessible locations, and these logs were combined with information from field-measured logs to build a 74 m thick composite log of the Sunset Cliffs locale (Figure 2E). The sand content, or 'net-to-gross', of a given package is the summed sand (net) thickness divided by the total (gross) thickness of the interval (e.g. Fryer & Jobe, 2019). Paleocurrents were measured from sole marks and ripple cross-lamination (Figure 2E), and the modal paleocurrent for each lobe complex was aggregated from all measurements within that complex. Lobe element and complex nomenclature follows Pyles et al. (2019), where Element 4-1 is the lowest (i.e. first) element of Lobe Complex 4.

5 | SEDIMENTARY FACIES

Six facies were identified in Sunset Cliffs and La Jolla based on grain size and sedimentary structures (Table 1) that are used to infer depositional processes. These facies provide evidence of the different types of sediment-gravity-flow deposits in the CLTZ, including mass-transport deposits (MTDs), high- and low-density turbidites, and hemipelagic deposits. Facies F1 is composed of structureless sandstone interpreted to be deposited as $S3/T_a$ divisions by high-density turbidity currents (Bouma, 1962; Lowe, 1982); abundant water-escape structures are evidence of very rapid deposition (Lowe, 1975). Facies F2 is composed of concave lamination that usually shallows in dip upward and is bounded by metre-scale truncation surfaces into 'sets'; these structures suggest deposition by unstable antidunes under a Froude-supercritical flow (Postma & Kleverlaan, 2018; Slootman et al., 2021). In some places, F2 sets contain abundant convolute lamination, evidence of rapid sedimentation. Facies F3 and F4 are generally T_{bcde} sandstone–mudstone couplets and represent low-density turbidity current deposits (Bouma, 1962; Walker, 1965). Facies F3 has >50% sand content compared to F4, which has <50%. Facies F5 consists of organic-rich mudstone that has common *Chondrites* and *Thalassinoides* burrows and occasional interbeds of current-ripple, cross-laminated sandstone; these low net-to-gross deposits are interpreted to represent hemipelagic deposition and occasional low-density turbidity currents. F6 generally

TABLE 1 Facies descriptions, interpretations and typical photographs. Scale card is 15 cm long in each photo.

Facies name	Description	Interpretation	Photograph
F1: Structureless, amalgamated sandstone	Medium to very coarse sandstone beds, 18–180 cm thick. Normally graded, structureless, common water-escape features (dishes), occasional soft sediment deformation and mud clast conglomerate	Deposited by high-density turbidity currents and represent the S3/Ta division (Lowe, 1982). Extensive fluidisation likely caused by rapid suspension sedimentation (Lowe, 1975)	
F2: Cross-stratified sandstone with soft-sediment deformation	Medium-grained to pebbly sandstone beds up to 3 m thick with abundant, low-angle lamination organised into sets bounded by truncation surfaces; some sets contain abundant soft-sediment deformation, mostly convolute lamination	Cross-stratified sets are likely antidune deposits from high-density, Froude-supercritical turbidity currents (Cartigny et al., 2014). Organised sets are likely aggradational antidunes, while the soft-sediment deformation was likely caused by migration of unstable, transient antidunes (Ono & Plink-Björklund, 2018)	
F3: Thin-bedded sandstone-mudstone	Interbedded sandstone (20–60 cm) beds and thin siltstone (5–15 cm). Sandstones show occasional graded bedding, parallel and ripple lamination and rarely sheared textures and mud clasts. Siltstones commonly bioturbated by *Chondrites*	Deposited by low-density turbidity currents and represent Tbcde divisions described by Bouma (1962) and interpreted by Walker (1965). Rarely, sand beds with sheared textures and mud clasts represent hybrid event beds (*sensu* Haughton et al., 2009)	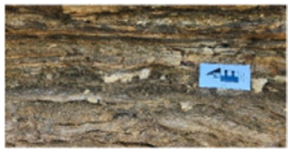
F4: Thin-bedded mudstone-sandstone	Organic-rich siltstones with occasional thin (1–5 cm) sandstone beds that are parallel and ripple laminated	Deposited by low-density turbidity currents and represent Tbcde divisions described by Bouma (1962) and interpreted by Walker (1965)	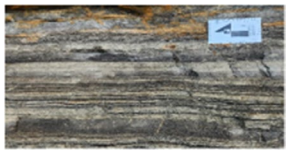
F5: Organic-matter-rich mudstone	Organic-matter-rich mudstone with occasional thin (3-5 cm) sand beds that are parallel and ripple laminated	Deposited in low-energy environment by hemipelagic deposition (Stow et al., 2001) and by occasional low-density turbidity currents (similar to F4)	
F6: Contorted mudstone	Heterogeneous mixture of sand, silt, and clay with chaotic laminations and clasts of both sandstone and mudstone up to 3 m long. Occasional bivalve and carbonaceous fragments	Deposited by a subaqeous mass failure as a mass-transport deposit (Bull et al., 2009). Bivalve and carbonaceous fragments suggest a shallow-marine source for the mass-transport deposit, but no detailed biostratigraphic analysis to confirm/deny this interpretation	

consists of contorted mudstone with raft blocks of sandstone and mudstone up to 3 m long and is interpreted as mass-transport deposits (e.g. Bull et al., 2009; Cardona et al., 2020; Nardin et al., 1979; Piper et al., 1997).

Facies associations were defined by grouping several facies that have been interpreted to be deposited in the same depositional setting; accordingly, facies are not exclusive to a single facies association. We identify five

TABLE 2 Facies associations and their depositional environment interpretations.

Facies Association	Facies	Sand content (net-to-gross)	Description	Interpreted depositional environment
FA1 Mudstone	F5, minor F4	<0.2	Mudstone, often organic-rich and bioturbated, with rare ripple-laminated sandstones less than 15 cm thick	Basin floor, distal lobe fringe or time period with no sand supply
FA2 MTD (Mass transport deposit)	F6, F5, F4, F3	Variable	Contorted, organic-rich mudstones with sandstone lenses and large (up to 3 m long) raft blocks. Extreme lateral variability in style and sand content	Distal lobe fringe, but likely sourced from further upslope in a bivalve-bearing shallow-marine environment
FA3 Mud-rich hetherolithic	F4, F5, F3	0.2–0.5	Mudstone with sandstone interbeds, sand content 15%–50%. Frequent pinch and swell in sandstones, and laterally transitions into FA4	Lobe fringe to off-axis
FA4 Sand-rich hetherolithic	F1, F2, F3, minor F4	0.5–0.8	Sandstones interbedded with thin mudstones generally continuous and tabular but can transition laterally into FA3	Lobe axis to off-axis
FA5 Amalgamated sandstone	F1, F2, minor F3	0.8–1.0	Sandstones with erosional, amalgamated bed contacts and common antidune deposits	Lobe axis or distributary channel

facies associations: mudstone (FA1), MTD (FA2), mud-rich heterolithic (FA3), sand-rich heterolithic (FA4) and amalgamated sandstone (FA5; Table 2). These facies associations are interpreted to represent different areas along the depositional profile (i.e. proximal to distal) and/or different positions within a lobe complex (i.e. axis to fringe), but lateral relationships between facies associations are generally not exposed in the study area. Rather, the vertical stacking defines changes in facies association and thus depositional environment.

6 | RESULTS: FACIES ARCHITECTURE

This study describes turbidites and MTDs at the Sunset Cliffs locale that were deposited in proximal (i.e. CLTZ) and distal lobe environments. These deposits are grouped hierarchically into mudstone-sheet, MTD, lobe, and channel architectural elements that stack to form Complexes 3, 4, 5, and 6. Complexes 1and 2 are located outside of the study area (Pyles et al., 2019). At Sunset Cliffs, Complex 3 consists of MTDs that stack to form an MTC. Complex 4 is interpreted as distal- to proximal-lobe deposits, and Complex 6 as proximal-lobe and channel deposits (i.e., channel-lobe transition zone). Complex 5 comprises a mudstone sheet of approximately 7 m thick that separates Complexes 4 and 6 (Figure 2A). Complexes 1–4 were previously described by Pyles et al. (2019), but Complexes 5 and 6 are newly documented in this study.

6.1 | Mass-transport Complex 3

The base of the measured interval is a *ca* 5 m thick MTC exposed at the Ladera Street staircase (MTC of Complex 4 of Pyles et al., 2019) that is extremely laterally variable in thickness and facies distribution (Figure 3). It consists of FA2 with highly contorted organic-rich mudstone (Figure 3C,D) with occasional sandstone lenses, 1–2 m mudstone raft blocks and areas of mud-clast conglomerate (Figure 3A,B). The MTC is composed of at least two mass-transport elements (sensu Pyles et al., 2019) that we interpret as individual mass-failure events (Figure 3C): a lower muddy, clast-rich unit with large (up to 2 m × 5 m) raft blocks and an upper sand-rich laterally variable unit that abruptly transitions northward from a tabular sandstone (Figure 3B,C) into mud-clast rich zones and contorted mudstone (Figure 3A,C). Even though this upper unit occasionally seems to be composed of undeformed turbidites (i.e. healing-phase deposits, Wood et al., 2015), these deposits are laterally variable and in some places contorted; thus, we interpret the entire package as the deposits of multiple mass-transport events (e.g. Bull

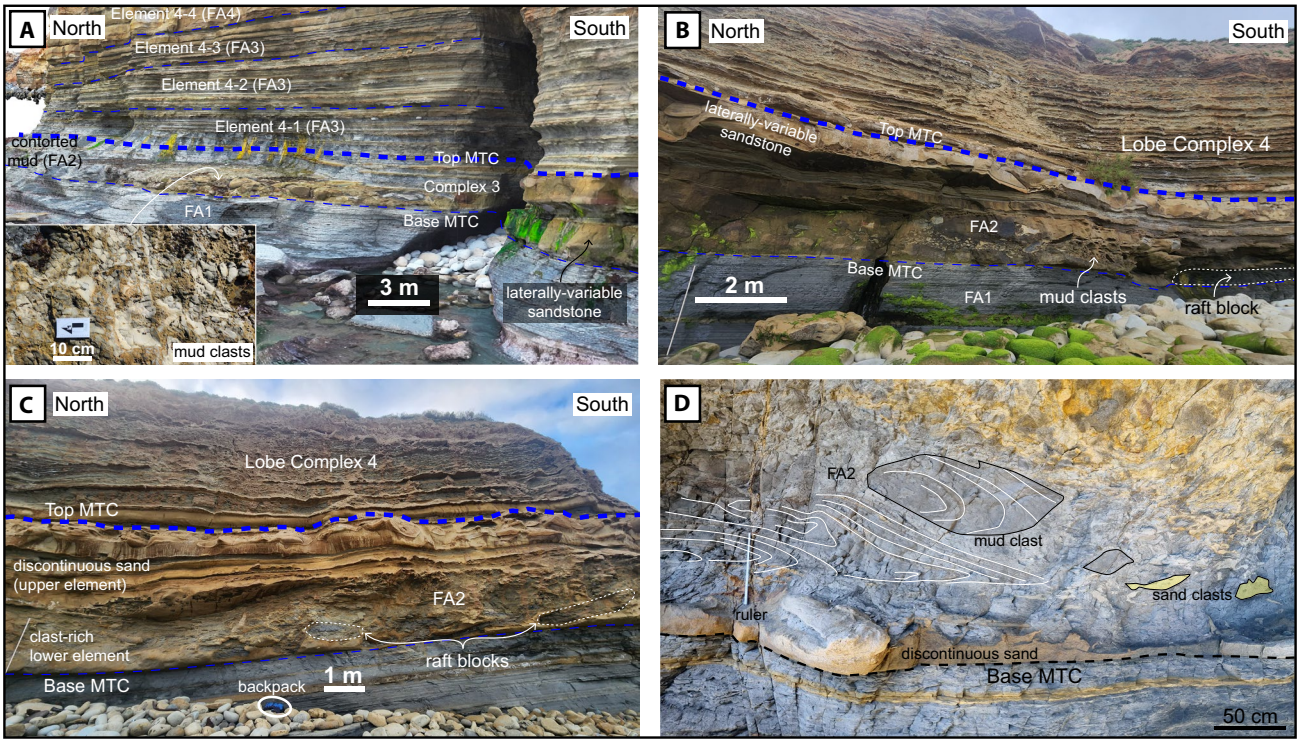

FIGURE 3 Mass-transport complex (MTC) of Complex 3 in Sunset Cliffs (see Figure 2A,D for location). (A) MTC lateral variability from sandy to mudclast-rich to contorted mudstone. (B) Basal clast-rich zone with large raft blocks overlain by bedded interval that is laterally variable. (C) Basal clast-rich zone and contorted sand-rich upper zone. (D) Contorted mudstone with sand and mud clasts, a few of which are highlighted.

et al., 2009) that have extreme spatial variability. The presence of shallow-water bivalve (oyster) shell fragments and abundant organic matter in this MTC suggests deposition from a shallow-marine source area. However, to the south of the staircase, the MTC can be traced into apparently undeformed FA3, suggesting that mass wasting deformed an existing distal-fringe or lateral-fringe lobe deposit, similar to observations from distal lobe deposits on the modern Congo Fan (Croguennec et al., 2017). Detailed biostratigraphic analysis of the MTC and surrounding units may shed light on these contradictory observations but is out of scope for this study.

6.2 | Lobe Complex 4

Lobe Complex 4 was deposited on top of the MTC of Complex 3 (Figure 4), with eight lobe elements that show progressively increasing net-to-gross (i.e. sand content) through time. This is particularly apparent in the lowermost four elements (Figure 4), where the sand content increases progressively from Element 4-1 to Element 4-4. Paleocurrent measurements are 315°–360°, similar to measurements of the same interval by Fleming (2010) and Pyles et al. (2019). The basal three elements (4-1, 4-2, 4-3) are each 2–2.5 m thick and composed of mud-rich FA3 (Figure 4A). Laterally, these three elements become progressively sandier (i.e. transition into FA4) over a 70 m distance northward (Figure 4B). Individual beds have visible pinch-and-swell geometries, comparable to beds documented by Kus et al. (2022).

Element 4–4 is recognisable as a package of FA4 with three distinct tabular sandstone beds of similar thickness that are traceable for more than 100 m north of the staircase (Figure 4A). A 20 cm thick mudstone separates these bedded sandstones from 5 m of amalgamated sandstone (FA5) that forms Element 4–5 (Figure 4C). Scour-and-fills with up to 1 m relief (Figure 4C) and soft-sediment deformation (Figure 4D) are present within the FA4 deposits of Element 4-5. There are no significant thickness and facies changes in this element.

Element 4-6 is well exposed near the Luscomb's Point 'cage' (Figures 2 and 5A), with high net-to-gross lenticular geometries (FA4 and FA5) bounded by erosional surfaces (Figure 5B,C) lined with mud clast conglomerate (Figure 5D,E). Paleoflow indicators in Element 4-6 are oriented northwest (Figure 5C), making this exposure an approximate dip panel. Element 4-7 is exposed just around the corner to the north in an approximate strike panel (Figure 6) and consists of metre-thick sandstone

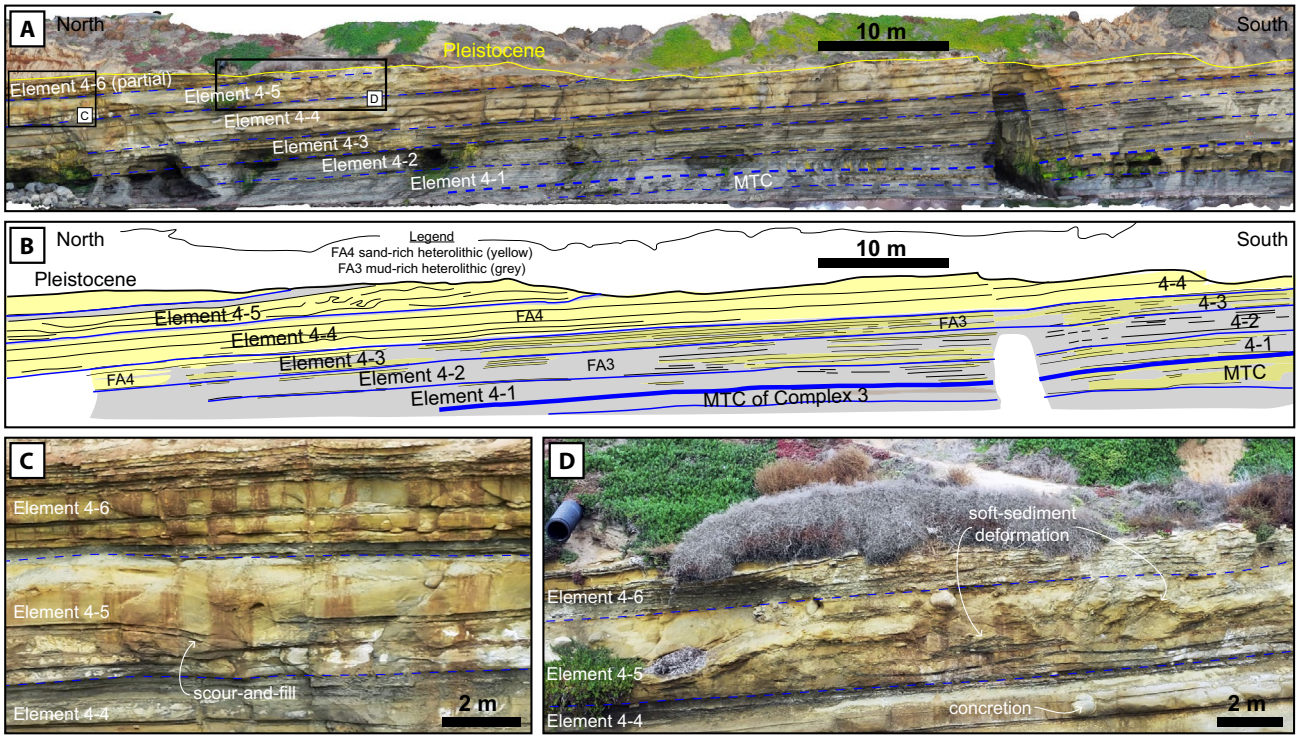

FIGURE 4 Complex 4 lobe deposits. (A) Photo and (B) line drawing of the vertical and northward increase in net-to-gross from FA3 to FA4 in the basal Elements 4-1 to 4-4. Elements 4-4 and 4-5 are composed of FA4 and transition northward into FA5. (C) Scour-and-fill and (D) soft-sediment deformation are common in Element 4–5, indicating rapid, sand-rich deposition.

beds that are amalgamated (FA5), several with prevalent soft-sediment deformation (Figure 6B) and water-escape features (Figure 6C). In particular, Figure 6C shows a well-exposed bed that has the classical upward progression of flat dishes to curved dishes to pillars (e.g. Fig. 18E of Lowe, 1976). Element 4-8 is the uppermost element of Complex 4 and marks a transition to muddier facies (Figure 6A).

6.3 | Complex 5 mudstone sheet

A mudstone (FA1) interval *ca* 7 m thick overlies Complex 4 and is exposed across the 170-m wide beach of 'Smuggler's Cove' (Figure 2A). This thickness is approximated as several normal faults cut through the observed cliffs and the thin-bedded nature of the unit makes across-fault correlation difficult. The lower contact is gradational, as Elements 4-7 and 4-8 become progressively muddier upward (Figure 6A), but the upper boundary is sharp, with amalgamated FA4 deposits of Lobe Complex 6 directly overlying the mudstone (Figure 7A). Most of the interval is structureless mud that is locally bioturbated, with interbedded thin (2–5 cm) sandstone beds that are parallel- to current-ripple-cross-laminated (Figure 7B). These sandstone beds become more frequent and thicker on-average to the north, but we did not quantify this relationship. Hybrid event beds are rare in Complex 5. Paleocurrents measured from current ripples in Complex 5 are directed northeast (Figure 7A), which differs somewhat from paleocurrents in Complexes 4 and 6 that are directed northwest (Figure 2E).

6.4 | Lobe Complex 6

Lobe elements in Complex 6 are comprised of alternating amalgamated sandstone (FA5) and heterolithics (FA4/FA3) and are generally more sand-rich than in Complex 4 (Figures 7A and 8). Paleocurrent measurements in Complex 6 show 225–360° with modal paleocurrent of 315° (Figure 8A). From base to top of the complex, there is an increase in the thickness of FA5 (Figure 2E). Element 6-1 sharply overlies the muddy FA1 of Complex 5 and consists of three tabular beds comprising a package of FA4 (Figure 7A). Element 6-2 consists of 9 m of amalgamated sandstone (FA5, Figure 7A) that is dominated by scour-and-fill features and bedforms interpreted here as antidunes (Figure 8A). Element 6-3 is *ca* 2 m thick and consists of mud-rich FA3, with sandstone beds that do not consistently thicken or thin upward (Figure 8A; cf. Prélat & Hodgson, 2013). This abrupt change in facies could be interpreted as a lobe complex boundary; we acknowledge that this is a fairly subjective decision, but we

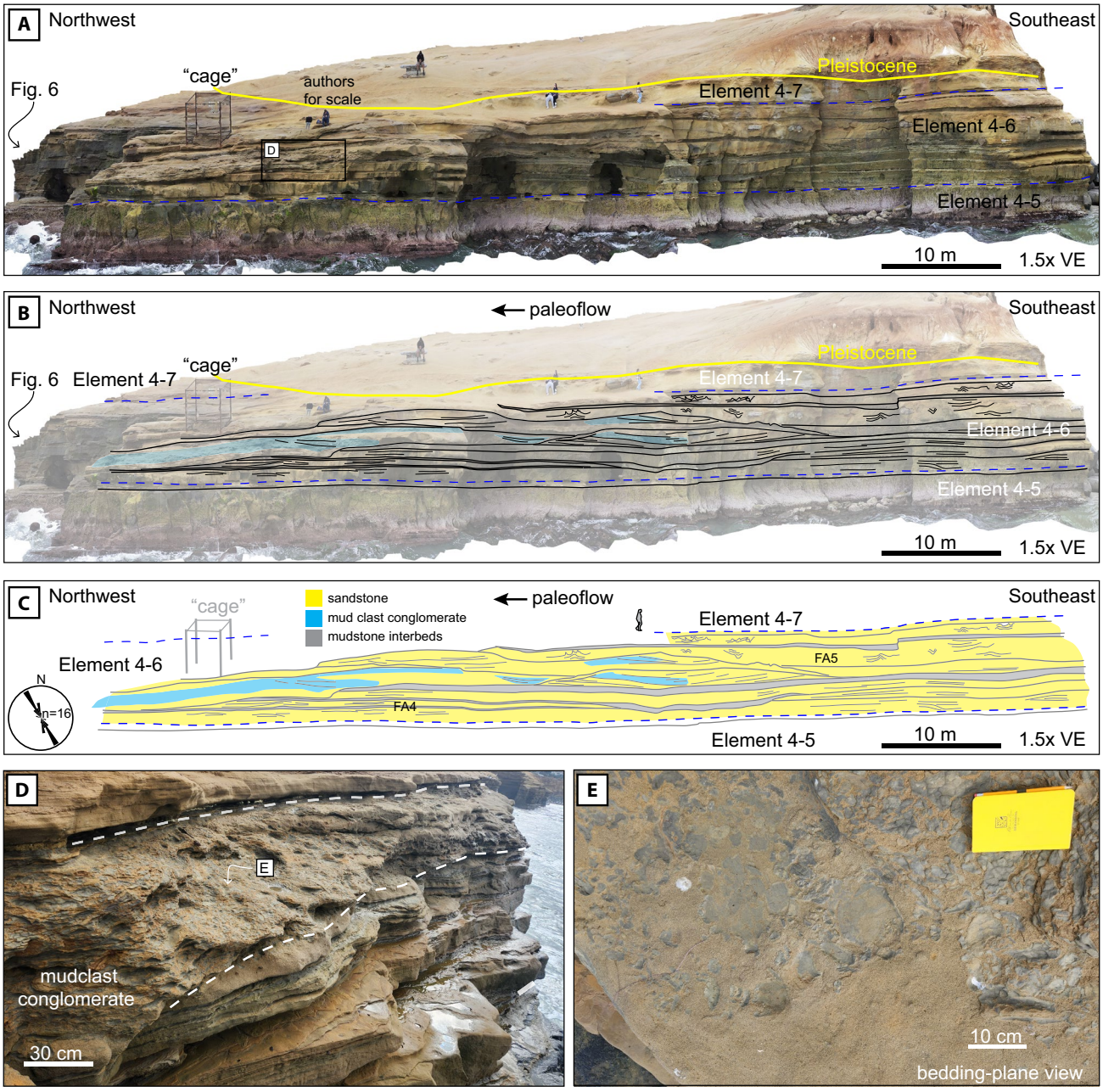

FIGURE 5 Lobe Complex 4, upper elements. Uninterpreted (A), interpreted (B), and line drawing (C) of Element 4-6 (1.5× vertical exaggeration; see location in Figure 2A). Many erosional surfaces are lined with mud-clast conglomerate, suggesting bypass along these surfaces. Note the paleocurrent indicators in part C suggesting this is a pure dip view (flow right to left). (D) and (E) show detailed photos of the mud-clast conglomerate near the 'cage'.

chose to keep all these elements in one complex because the amalgamated facies below (Element 6-2) and above (Element 6-4) are quite similar. Element 6-4 has a basal amalgamated zone with mud clasts (Figure 8A) and an upper tabular sandstone, with no apparent facies change northward.

Element 6-5 erodes into the top of Element 6-4 and is composed of FA4 and FA5 with metre-scale soft-sediment deformation features (Figure 8B inset). A mud-rich heterolithic interval *ca* 50 cm thick is eroded to the north (Figure 8B) and zones of mud clasts are common. The base of Element 6-6 is also erosional, with *ca* 1 m of relief (Figure 8B). Throughgoing scour surfaces in FA5 are common in this element, some surfaces are lined with large sand and mud rip-up clasts (Figure 8C). Element 6-7 is composed of FA5 and has well-exposed bedforms interpreted here as unstable antidune deposits (Figure 9). The final element that we describe is Element 6–8, which is exposed near the 'yoga terrace' (Figures 1 and 2). This element is composed of FA4 with abundant

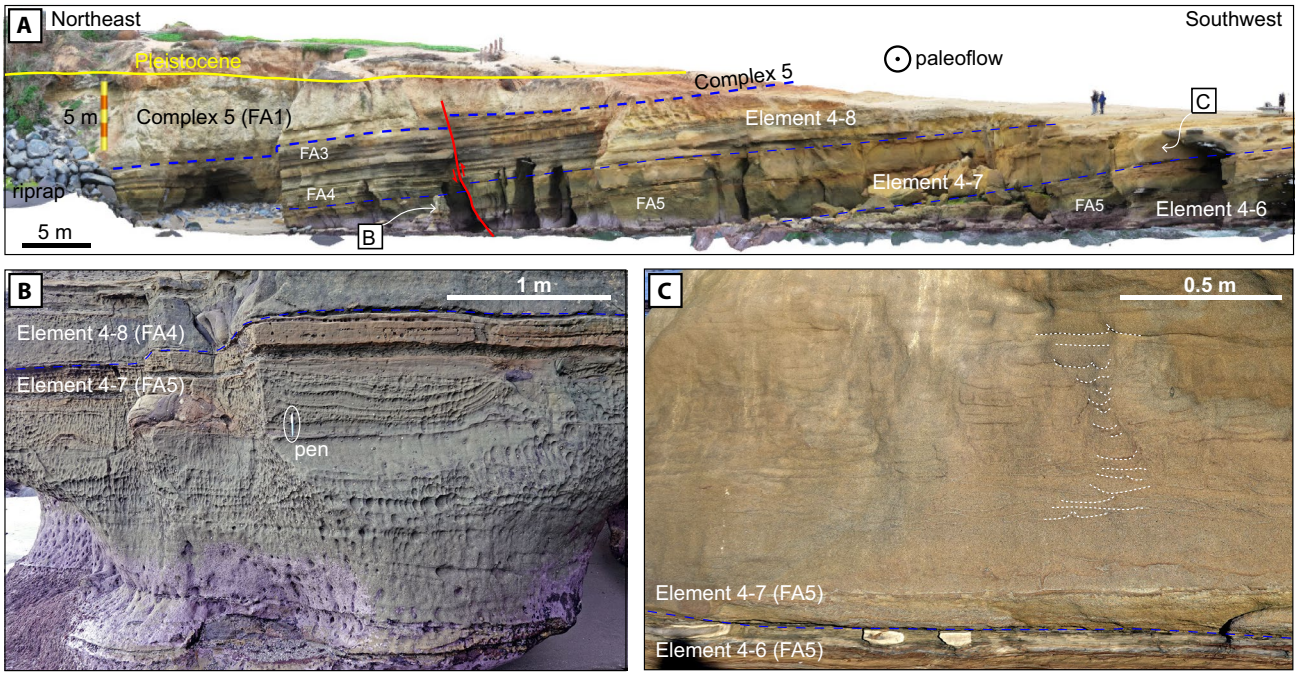

FIGURE 6 Upper elements of Lobe Complex 4. (A) Strike-oriented panel showing the progressive upward decrease in sand content from FA4 to FA3 in Element 4–8 and into FA1 of Complex 5. (B) and (C) show the pervasive soft-sediment deformation and water-escape structures (a subset of which is highlighted in white) in the high net-to-gross FA5 deposits of Element 4-7 (see locations in part A).

soft-sediment deformation, from convolute lamination common at bed tops to meter-scale folds (Figure 9A). The top of Element 6-8 is poorly exposed in a small cove adjacent to the farthest-north parking lot along Sunset Cliffs, and the overlying strata are also poorly exposed and inaccessible. Farther north, there is a seawall and riprap that prevents further exposure of the Point Loma Formation.

6.5 | Quantification of scour dimensions

Scours commonly form in transitional zones where slope channels transition to base-of-slope proximal lobes (Carvajal et al., 2017; Kane et al., 2009; Normandeau et al., 2025). This setting has been inferred to promote erosion of the bed and induce hydraulic jumps as flows become unconfined (Kane et al., 2009; Komar, 1971; Macdonald et al., 2011). Scour fields and scour-and-fill structures have been observed in channel–lobe transition zones (Normandeau et al., 2025; Pemberton et al., 2016; Symons et al., 2016) and have been reported at abrupt breaks in slope (Wynn et al., 2002). Generally, autogenic scours are thought of as occurring during aggradation of a bed due to flow turbulence, and allogenic scours are longer-lived features that represent the bypass of turbidity currents (Kane et al., 2009).

Erosional surfaces (i.e. scours) are common in the study area (e.g. Figures 5 and 10) and were mapped in VRGS (software described in the methods section) for the total vertical relief (i.e. depth) and total horizontal dimension (i.e. apparent width). The scours in Complexes 4 and 6 generally have dimensions of <1 m relief and 1–100 m width (Figure 10C) and are here interpreted as autogenic scours (e.g. Jobe et al., 2012; Kane et al., 2009) because they generally lack the substantial mudstone drapes associated with allogenic scours (e.g. Elliott, 2000). The scour-and-fill deposits in Sunset Cliffs (e.g. Figure 10B) may be the depositional product of a series of cyclic steps (cf. Englert et al., 2021; Ono & Plink-Björklund, 2018), but mapping these deposits in 3D is not possible due to outcrop constraints. Element 4-6 typifies the scour geometries and surrounding facies architecture (Figure 10). Scours in the study area closely match the scaling relationships defined by Kane et al. (2009) of approximately 10:1 width: depth ratio (Figure 10C). Because the measurements are taken along the outcrop in oblique orientations to the paleoflow, this width:depth ratio might be somewhat over- or underestimated in some cases, but the similarity with the data of Kane et al. (2009) suggests the scour dimensions from the Point Loma Formation are representative. The depth of scouring in the study area suggests a lower-gradient, channel-lobe-transition-zone setting (e.g. Carvajal et al., 2017), but the lack of other exposure precludes

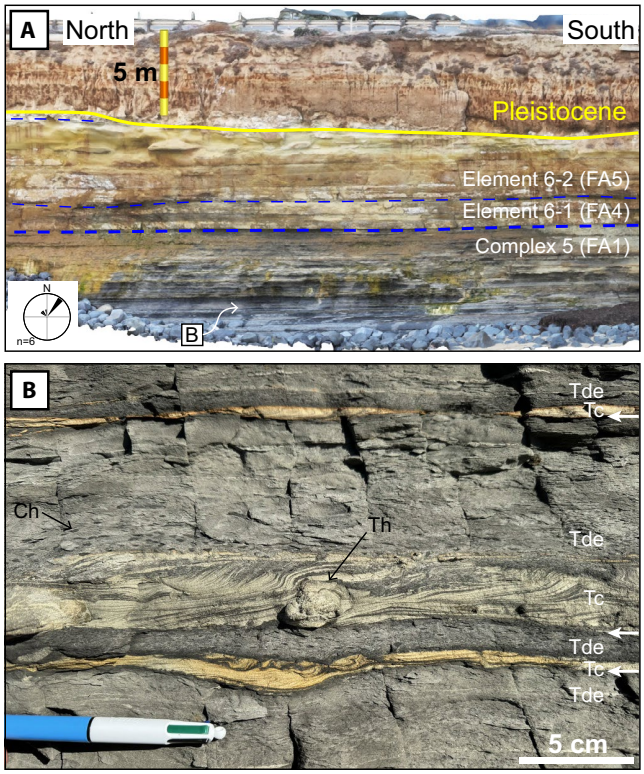

FIGURE 7 Complex 5 mudstone 'sheet'. (A) Digital outcrop model showing the upper part of this low (15%) net-to-gross package that is composed predominantly of mudstone (FA1). Note the sharp upper contact with Complex 6, likely representing an abrupt compensational shift in deposition. (B) Detailed photo showing thin interbedded sandstones that are current-ripple, cross-laminated (Tc turbidite divisions, bed bases shown with white arrows) and locally convoluted. Bioturbation shown with black arrows (Th = Thalassinoides; Ch = Chondrites). Bic 4-colour pen for scale.

observations of larger scours that are commonly mapped on the seafloor (e.g. Normark et al., 1979) and in better-exposed outcrop areas (e.g. Hofstra et al., 2015).

6.6 | Supercritical-flow sedimentary structures at Sunset Cliffs

The interpretation of sedimentary structures in terms of formative flow conditions is often speculative when supercritical flow is inferred because of the spatiotemporal complexity of erosion and deposition in such flows. However, flume experiments have provided insights into the relationships between flow regime and the erosional and depositional character of laminations that may be preserved (Kennedy, 1963; Simons & Richardson, 1961). Experimental antidunes typically form in trains marked by the occasional breaking of in-phase waves generating scour-and-fill structures in both fluvial flows (e.g. Alexander et al., 2001; Cartigny et al., 2014) and density currents (Fedele et al., 2016; Hand, 1974; Lang, Brandes, & Winsemann, 2017). Higher aggradation rates, for example, as a result of rapid loss of flow capacity at the break in slope (Tinterri, 2025), lead to increased preservation of convex lamination (Cartigny et al., 2014; Lang, Brandes, & Winsemann, 2017; Lang, Sievers, et al., 2017; Slootman et al., 2021). Discrimination of antidune deposits from sedimentary structures formed by other supercritical-flow bedforms, in particular cyclic steps that are formed by trains of hydraulic jumps, is often problematic (Hughes Clarke, 2016; Ono & Plink-Björklund, 2018; Postma et al., 2009; Slootman & Cartigny, 2020).

Amalgamated sandstone packages in the Sunset Cliffs area are commonly 2–5 m thick, relatively tabular and are bounded by laterally persistent, thin (<10 cm) mudstones (e.g. Figure 9C); Element 6-2 typifies this depositional style (Figure 11A). Within these sandstone packages, organised, low-angle lamination is common with dominant orientations down-paleoflow (i.e. foresets) and up-paleoflow (i.e. backsets). Both concave and convex lamination are preserved, indicating high aggradation rates (Figures 11A,B and 12D; also see Cartigny et al., 2014; Fielding, 2006; Lang, Brandes, & Winsemann, 2017). The concave laminae taper in thickness to form crests with wavelengths up to several meters (Figures 9C and 11A; also see Slootman et al., 2021). Internal truncations with <1 m of relief separate and define sets that are lenticular (Figure 9). Set boundaries are, in some places, defined by a 10–50 cm thick package of convolute-laminated sandstone (Figures 11A and 12D; cf. Postma et al., 2009). Grain size within sets is generally well-sorted (e.g. faint lamination in upper set of Figure 11A), but sharp grain-size changes occasionally occur at set boundaries (Figure 11B,C), and particularly when convoluted-lamination is present (e.g. Figure 12D; cf. Postma et al., 2009). These low-angle laminations are commonly truncated at the top of the package, forming a sharp, planar upper boundary (Figures 9C and 11B). Some units have more organised sets with predictable lamination orientations (Figures 9 and 11A) while others are more chaotic, with set boundaries defined by sharp, angular scour surfaces (Figure 11B) and less continuous lamination style (Figure 11C).

We interpret these tabular sandstone packages as single event beds containing the depositional products of aggrading and migrating antidunes (e.g. Lang, Brandes, & Winsemann, 2017; Lang, Sievers, et al., 2017; Ono & Plink-Björklund, 2018; Postma et al., 2021). The bed shown in Figure 9C typifies this style, with at least eight sets that represent the spatial and temporal migration of antidunes during deposition. The continuous, wavy laminations within a set (Figure 11A) indicate deposition by antidunes with strongly aggradational crests, while more chaotic units may be (1) lower-aggradation

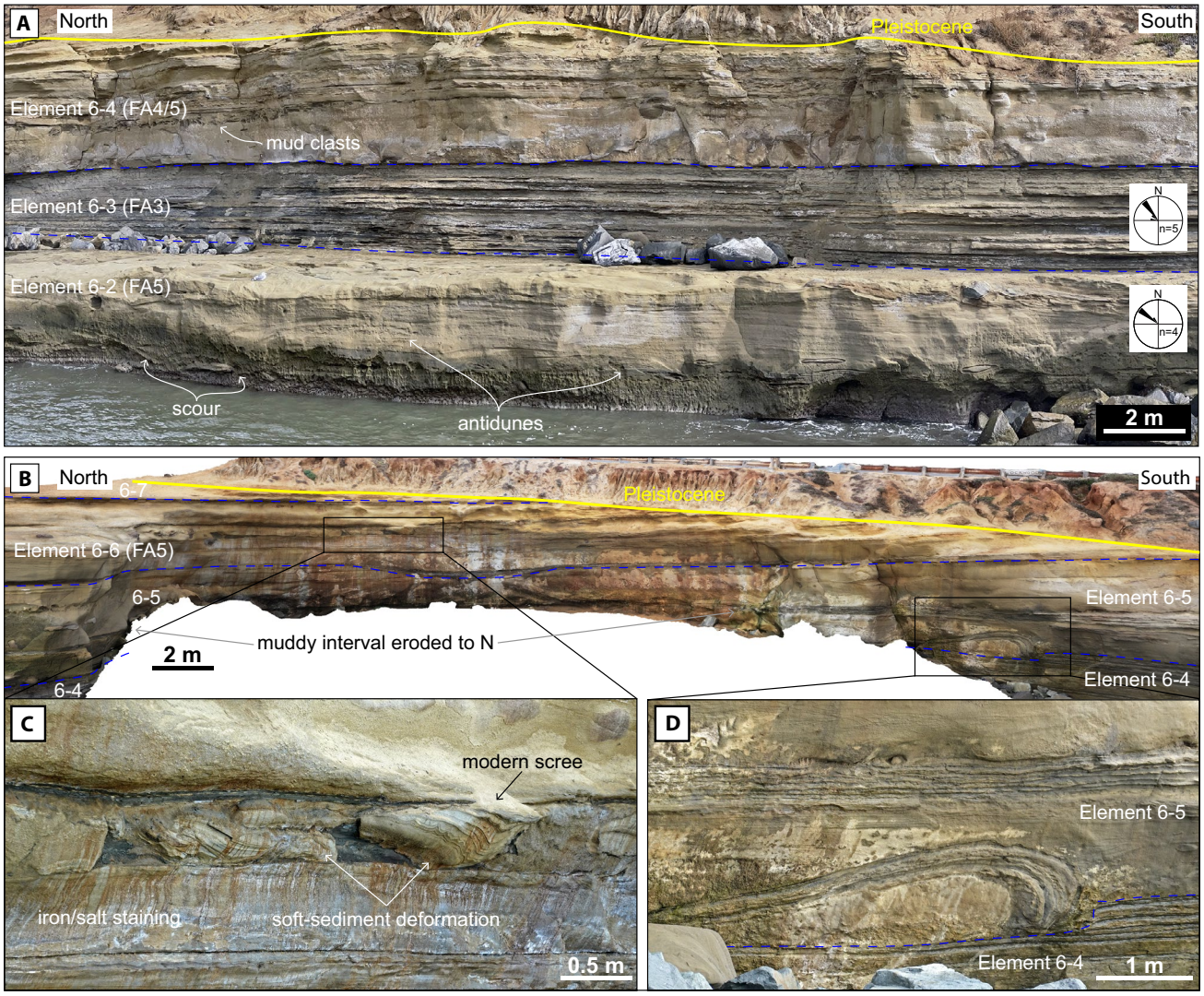

FIGURE 8 Lobe complex 6 (see location on Figure 2). (A) Antidunes and scour-and-fill structures in Element 6-2 are overlain by mud-rich Element 6-3 and sand-rich and amalgamated deposits in Element 6-4. (B) Elements 6-5 and 6-6 are composed of FA4 and FA5 and are >90% net-to-gross. (C) Localised soft-sediment deformation in Element 6-5 and (D) zones of rip-up clasts in Element 6-6 both suggest bypass, rapid sedimentation and the presence of a nearby (perhaps local) slope.

rate antidunes, or (2) unstable antidunes associated with wave breaking and transient hydraulic jumps. The transient, unstable nature of these bedforms is corroborated by the presence of convoluted laminations that commonly occur along erosional set boundaries (Figures 11A and 12C); this is also observed in experiments of breaking-wave (i.e. unstable) antidunes (Alexander et al., 2001; Cartigny et al., 2014). We do not observe well-organised backsets with parallel set boundaries that indicate deposition by a more organised migrating train of cyclic steps (e.g. Yokokawa et al., 2009; see also Slootman & Cartigny, 2020).

The aforementioned antidune deposits are most prevalent in Complex 6. In Complex 4, antidunes are less common in tabular sandstone packages. However, Element 4-6 contains several exposures of nested scour-and-fill features at a larger scale (Figures 5 and 10B) that likely represent cyclic-step deposits that are larger and less aggradational than antidunes (Englert et al., 2021; Ono & Plink-Björklund, 2018). The scour surfaces are also commonly draped with thin mudstones (Figure 10B), suggesting more intermittent flow (cf. Postma et al., 2021) as compared to the amalgamated deposits of Complex 6 (e.g. Figure 9C).

6.7 | La Jolla locale

Outcrops of the Point Loma Formation at La Jolla (Figure 1) have quite similar facies to those found in Sunset Cliffs. At the 'Wipeout Beach' locale, a particularly well-exposed, 19 m thick, continuous section

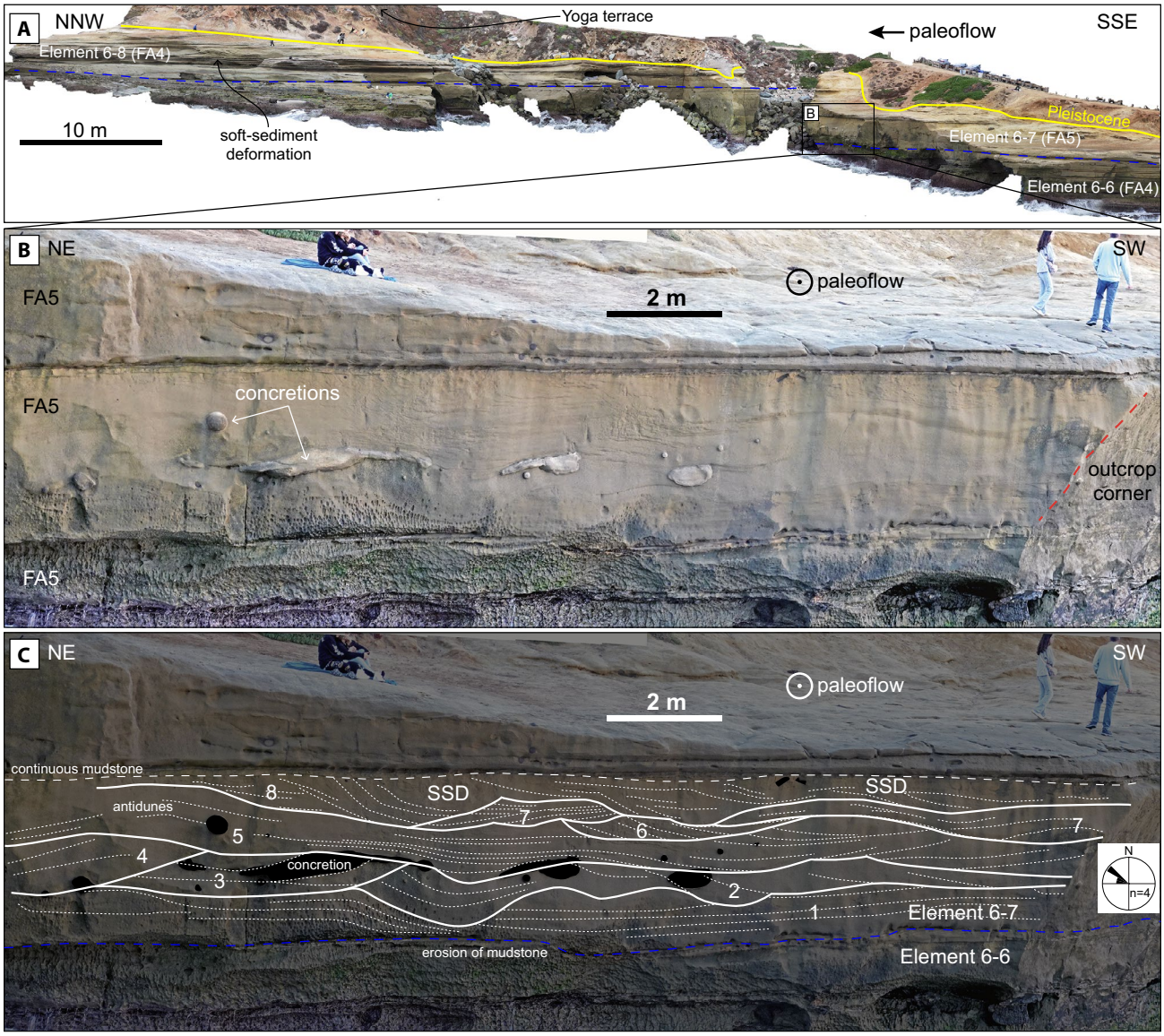

FIGURE 9 (A) Northernmost exposures of Complex 6, where Elements 6-7 and 6-8 are exposed. Uninterpreted (B) and interpreted (C) cliff-face of Element 6-7, oblique to part A. This interval has at least eight surface-bounded (numbered) sandstone sets interpreted as aggradational, unstable antidune deposits (paleoflow out of the page). SSD indicates soft-sediment deformation. Note the diagenetic concretions are shaded black in part C.

(Figure 12) contains supercritical-flow structures in amalgamated sandstone deposits (FA5) interbedded with mud-dominated heterolithics (FA3) that are quite analagous to the deposits of Complex 6 at Sunset Cliffs. Six elements are interpreted at Wipeout Beach (here named elements LJ1–LJ6 to avoid confusion with the elements in Sunset Cliffs), with amalgamated sandstones 2–4.5 m thick (Figure 12B). Bedding-plane exposures of current ripples at Wipeout Beach and in outcrops *ca* 500 m to the south provide paleocurrent measurements ($n = 18$) that trend southeast (Figure 12), opposite that of Complexes 4, 5 and 6 in Sunset Cliffs. The uppermost element at Wipeout Beach is well-exposed along a wave-cut platform that allows a quasi-3D view of the supercritical-flow deposits (Figure 12B,C). This dip-oriented exposure displays bedform wavelengths on the order of 5 m and contains more preserved foresets than backsets, given the southward paleoflow (Figure 12C). It is difficult to trace some bed boundaries, demarcated by extensive soft-sediment deformation, for more than approximately 25 m (red lines in Figure 12C), suggesting very rapid sedimentation. Locally, soft-sediment deformation includes large flame structures, which are typical for deposition under hydraulic jumps in cyclic steps (e.g. Postma et al., 2009). Some thicker sets with steeper cross bedding associated with large flame structures are

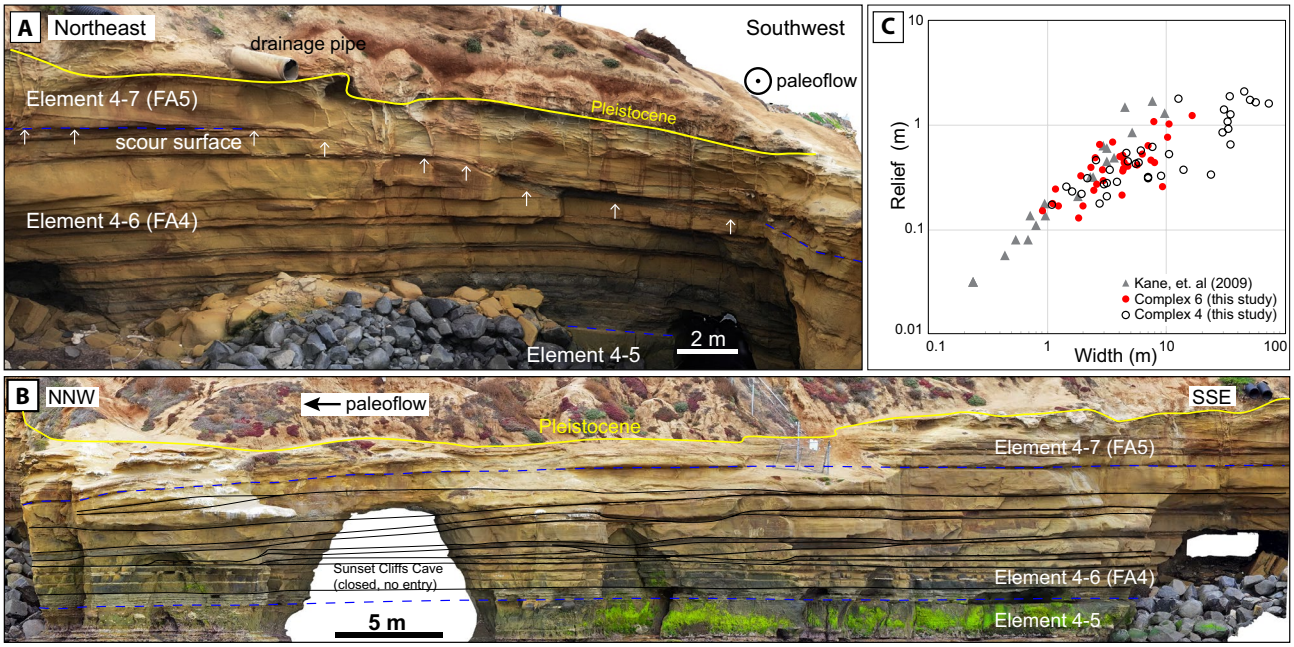

FIGURE 10 Scours in channel–lobe transition zone (CLTZ) deposits of the Point Loma Formation. (A) Strike view of scour surfaces in Complex 4. The base of Element 4-7 has approximately 2 m relief, with a composite surface that suggests prolonged bypass during its development. (B) Dip view of the same interval, showing nested scour-and-fill features in Element 4–6 and the relief on the base of Element 4–7. (C) Scour dimensions from Complexes 4 and 6 compared to the megaflute dataset of Kane et al. (2009), indicating very similar scaling relationships among the three datasets.

hence interpreted as cyclic-step deposits (Figure 12D), whereas thinner sets with more gentle lamination represent deposition by unstable antidunes (cf. Figure 11A) (Ono & Plink-Björklund, 2018; Postma et al., 2009; Slootman & Cartigny, 2020).

The lack of exposure created by the syncline that forms Mission Bay (Figure 1), insufficcient pre-Cretaceous bathymetry information, and the absence of high-precision geochronology prevent any detailed complex-scale or element-scale correlation between Sunset Cliffs and the Wipeout Beach locale at La Jolla that are *ca* 12 km apart. Future work should focus on better characterisation of the La Jolla exposures, a more precise correlation between the two areas, and an updated paleogeographic reconstruction to better constrain the divergence in paleoflow.

7 | DISCUSSION

7.1 | Depositional processes and bedform dynamics in the CLTZ

Outcrop studies (Brooks et al., 2018, 2022; Englert et al., 2021; Hofstra et al., 2015, 2018; Ito, 2008; Mansor & Amir Hassan, 2021; Pemberton et al., 2016; Postma et al., 2021) have helped develop recognition criteria for CLTZs, a site of rapid flow expansion (Macdonald et al., 2011; Pohl et al., 2020) due to a decrease in confinement or a gradient change at the base of the slope (Mutti & Normark, 1987). Erosional scours are commonly developed in this zone due to the formation of hydraulic jumps (Ito, 2008; Macdonald et al., 2011; Postma et al., 2021; Wynn et al., 2002). This study reaffirms the presence of hydraulic jumps and associated supercritical-flow sedimentary structures (e.g. interpreted antidunes) in CLTZ deposits (Lobato et al., 2025; Ono & Plink-Björklund, 2018; Postma et al., 2009, 2021; Postma & Cartigny, 2014; Postma & Kleverlaan, 2018; Sapardina, 2023). These deposits are typified by low-amplitude, concave and convex lamination, scour-and-fill structures and backset bedding (Ono & Plink-Björklund, 2018; Slootman et al., 2019). Erosional surfaces define 'sets' that are trough-shaped with crescentic or oval planform geometries, and with lenticular, sigmoidal/wedge-shaped or tabular in cross-sections (Englert et al., 2021; Hage et al., 2018). The sets are the record of upslope bedform movement, although the whole bedform amplitude might be difficult to determine in partially eroded sedimentary structures (Figure 11; Slootman & Cartigny, 2020). Subsequent sets are commonly offset upslope forming low-angle backset stacking patterns (Englert et al., 2021), comparable to

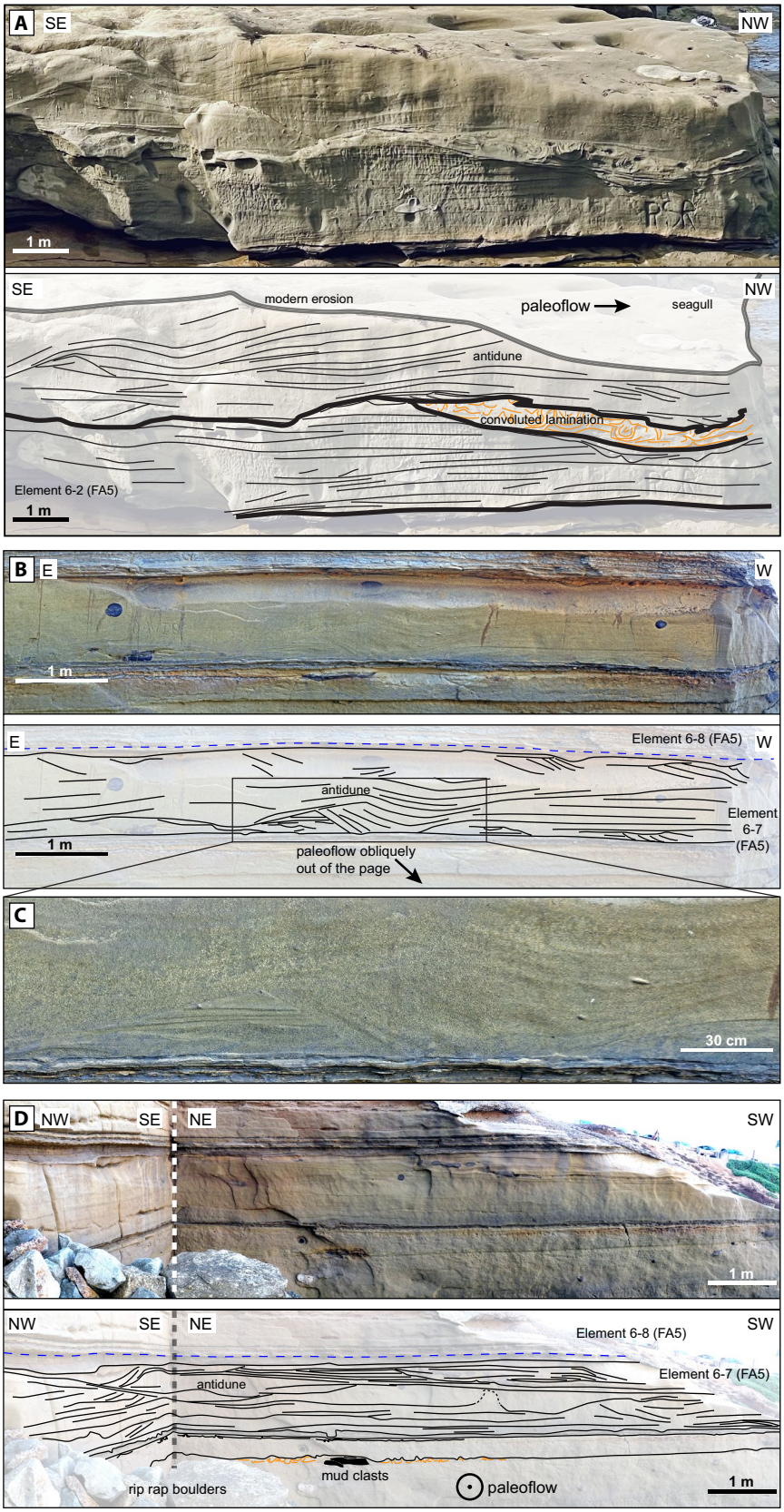

FIGURE 11 Aggradational, migrating and unstable antidunes in FA5. (A) Aggradational antidune deposits in Element 6-2; note the package (i.e. set) of convolute bedding, suggesting unstable or breaking behaviour. See location in Figure 1, adjacent to deposits shown in Figure 8A. (B) and (C) show the grain-size variability between antidune sets in Element 6-7, also commonly seen in modern and experimental datasets. (D) Partial 3D view of antidune deposits in Element 6-7, suggesting that these bedforms had complex 3D morphologies. See location of parts B, C, and D in Figure 1, adjacent to deposits shown in Figure 9A.

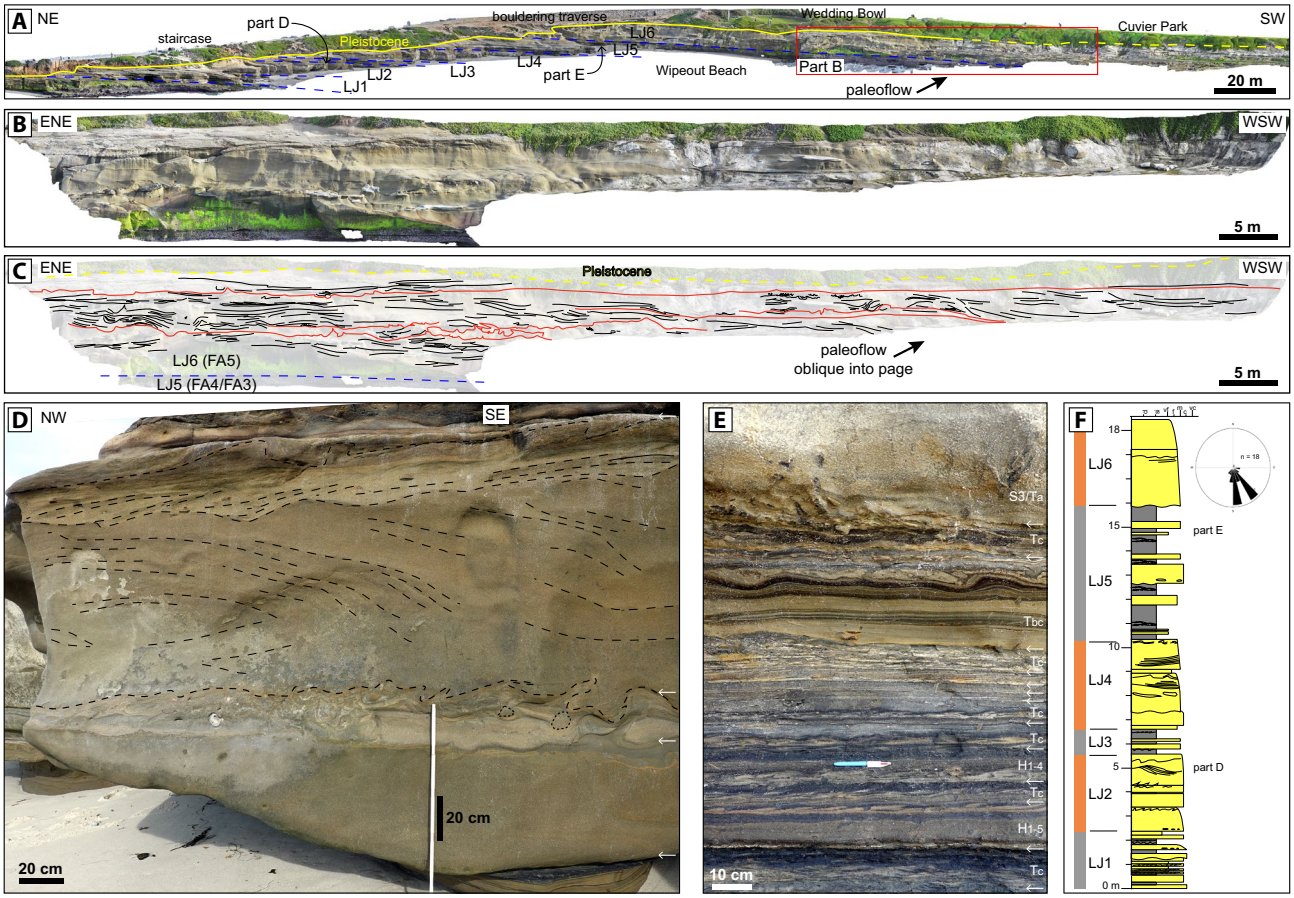

FIGURE 12 CLTZ elements at La Jolla area. (A) Orthomosaic overview of the 500-m wide Wipeout Beach section where six elements are delineated: LJ1–LJ6. Uninterpreted (B) and interpreted (C) orthomosaic photo panels of scour-and-fill deposits of Element LJ6 interpreted as supercritical-flow deposits. (D) Meter-thick sandstone package in Element LJ2 with well-expressed lamination likely formed by cyclic steps overlain by antidune deposits. The loaded base and top suggests rapid deposition. White arrows mark event bed boundaries. (E) Mud-rich heterolithic deposits of Element LJ5, with interbedded turbidites and hybrid event beds and plentiful bioturbation. (F) Graphic log of the elements exposed in part A, with paleocurrent data from Element LJ6 and exposures 500 m to the south of Wipeout Beach.

the geometries seen in Figure 11A. The antidune structures in the Point Loma Formation are generally smaller than the stratigraphic products of time-lapse bathymetric surveys of the modern seafloor, suggesting either smaller formative bedforms due to differences in slope gradient or flow thickness (Slootman & Cartigny, 2020) or a bias of comparing outcrop and bathymetry datasets (Englert et al., 2021). However, the organised scour-and-fill deposits of Element 4-6 (Figure 10) are similar in scale to the cyclic-step deposits from the Squamish and Monterey systems shown by Englert et al. (2021), although a quantitative comparison has not been made.

7.2 | Paleogeographic reconstruction and stratigraphic evolution

The Point Loma Formation has been interpreted as a submarine fan comprised of four lobe complexes (Fleming, 2010; Pyles et al., 2019). This study documents two additional complexes in the northern Sunset Cliffs area, specifically the muddy Complex 5 and the sand-rich Complex 6 with abundant antidune deposits. Therefore, we propose an update to the paleogeographic reconstruction of the Point Loma Formation to include all of the six complexes (Figure 13). We will only discuss the deposition of Complexes 4, 5, and 6 in this section and refer the reader to Pyles et al. (2019) for the evolution of Complexes 1, 2, and 3.

In tectonically active basin margins, the slope may be consistently above-grade and unstable, allowing mud-rich substrate to be both entrained as mud clasts and remobilised as MTCs (e.g. Brooks et al., 2022). The 2 m thick MTC that forms the upper part of this study's Complex 3 (see Table 3 for nomenclature clarification with Pyles et al., 2019) transitions laterally from deformed sand-rich facies into seemingly non-deformed mud-rich heterolithic facies (Figure 4), suggesting that this MTC may not have been an extensive

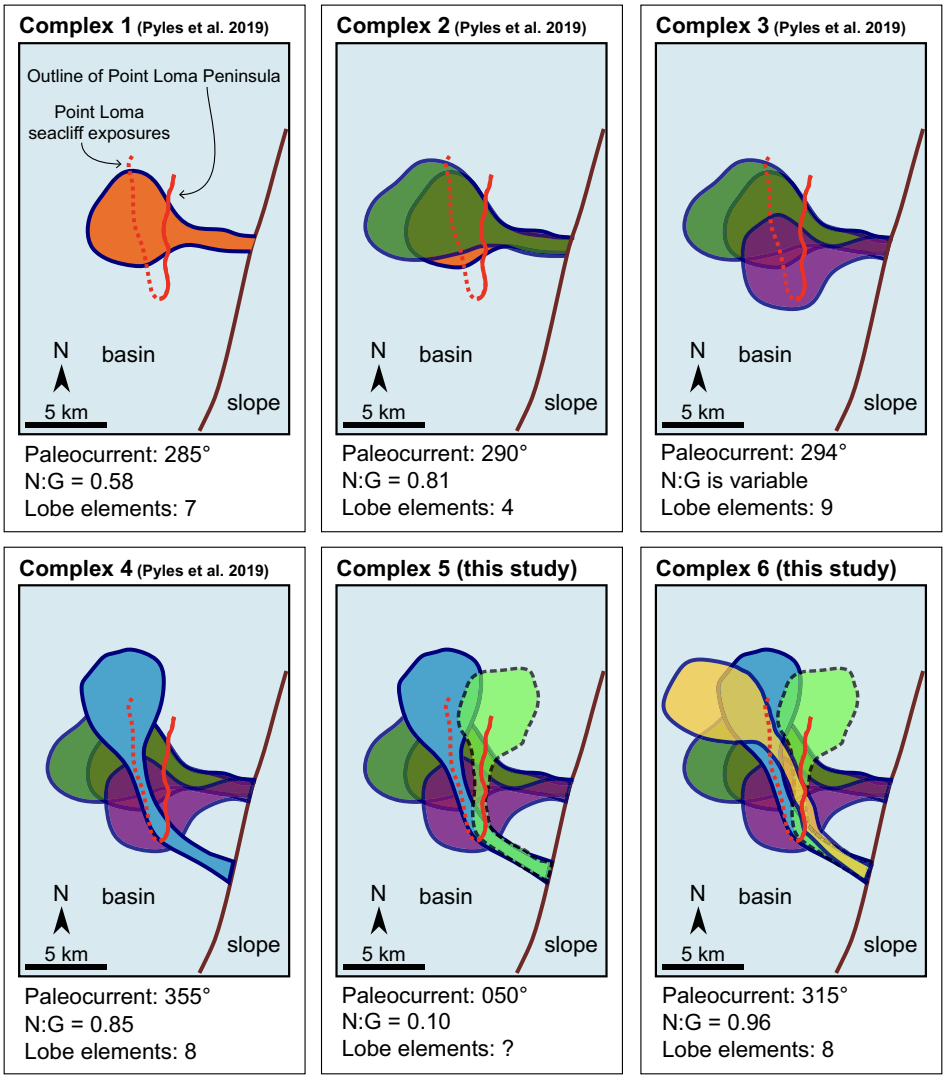

FIGURE 13 Paleogeographic reconstruction of the Point Loma Formation lobe complexes (modified after Pyles et al., 2019). This study adds the estimated locations of Complexes 5 and 6. While the location of Complex 6 is confident, the dashed line for Complex 5 indicates uncertainty for the environment of this mud-rich complex.

basin-wide deposit, but rather a lateral (or distal) facies transition at a lobe-fringe position. These facies changes have also been documented in modern-seafloor deposits in channel-lobe transition zones and in lobe environments (Carvajal et al., 2017; Dennielou et al., 2017; Talling et al., 2010; Twichell et al., 1992). However, the presence of oysters in the MTC does suggest a shallow-marine source area, suggesting potentially a more proximal slope position. Thus, predicting the exact environment of deposition for this MTC is quite difficult, and would require focused study and biostratigraphic analysis.

On top of the MTC of Complex 3, the lower four elements of Lobe Complex 4 are fairly tabular and comparatively muddier than the overlying elements, suggesting an off-axis or fringe position in an idealised lobe complex (Figure 13; Deptuck et al., 2008; Nilsen & Abbott, 1981; Prélat et al., 2009; Pyles et al., 2019). The lack of hybrid event beds in these elements suggests a lateral rather than distal fringe location (Spychala et al., 2017). The progressive vertical and northward increase in sand content in Elements 4-1 to 4-4 (Figure 4) suggests a lateral compensation toward the axis of the lobe complex through time. However, the outcrop orientation is oblique to the Complex 4 paleoflow direction, so there may be a component of forward progradation as well (e.g. Prélat & Hodgson, 2013). Extensive soft-sediment deformation in Element 4-5 (Figure 4) is comparable to distal-lobe deposits of the Congo Fan (Dennielou et al., 2017) and suggest a local slope nearby and/or persistent shear from overlying flows that disrupts underlying stratigraphy (cf. Van Der Merwe et al., 2009). The erosional surfaces, scour-and-fill, and amalgamated sandstone facies in Element 4-6 indicate balanced erosion and

TABLE 3 Stratigraphic comparison of this study to previous study by Pyles et al. (2019).

Lobe complex (Pyles et al., 2019)	Lobe element (Pyles et al., 2019)	Facies architecture at Sunset Cliffs	Lobe element (this study)	Lobe complex (this study)
Not studied		Amalgamated sandstone with large-scale soft-sediment deformation (FA4)	Element 8	Complex 6
		Amalgamated sandstone with antidunes (FA4–FA5)	Element 7	
		Amalgamated sandstone (FA5)	Element 6	
		Amalgamated sandstone with large-scale soft-sediment deformation (FA4)	Element 5	
		Amalgamated sandstone (FA4–FA5)	Element 4	
		Thin-bedded mudstone-sandstone (FA3)	Element 3	
		Thick amalgamated sandstone with antidunes (FA5)	Element 2	
		Medium-thick tabular sandstone (FA4)	Element 1	
		Mudstone interval (FA1)	Not split into elements	Complex 5
Complex 4	Element 8 (C4_8)	Interbedded sandstone-mudstone (FA4–FA3)	Element 8	Complex 4
	Element 7 (C4_7)	Amalgamated sandstone (FA5)	Element 7	
	Element 6 (C4_6)	Amalgamated sandstone with scour-fill architecture (FA4 and FA5)	Element 6	
	Element 5 (C4_5)			
	Element 4 (C4_4)			
	Element 3 (C4_3)			
	Element 2 (C4_2)	Amalgamated sandstone (FA5)	Element 5	
	Element 1 (C4_1)	Medium-thick tabular sandstone (FA4)	Element 4	
Complex 3	Element 8 (C3_8)	Thin-bedded mudstone-sandstone (FA3)	Element 3	
	Element 7 (C3_7)	Thin-bedded mudstone-sandstone (FA3)	Element 2	
	Element 6 (C3_6)	Thin-bedded mudstone-sandstone (FA3)	Element 1	
	Element 5 (C3_5)	Exposed at Cabrillo National Monument (Fryer et al., 2021; Pyles et al., 2019)	Not present at Sunset Cliffs	Not present at Sunset Cliffs
	Element 4 (C3_4)			
	Element 3 (C3_3)			
	Element 2 (C3_2)			
	Element 1 (C3_1)			
Mass transport complex (MTC)	Various elements, see Pyles et al. (2019)	Contorted bedding, large sand and mud raft blocks, extreme variability	Not split into elements	Complex 3

deposition patterns typical in the development of the CLTZ, and similar to 'pre-channel proximal-lobe deposits' defined by Pickering et al. (2015). Element 4-7 is the most amalgamated element in Complex 4 (Figure 6) and likely records the most axial position (Figure 13) before a shift to off-axis deposits of Element 4-8, and finally, a cessation of sand-rich sedimentation recorded by Complex 5. In the upper part of Complex 4, the progressive shift to more erosional and

amalgamated facies before a final change to lower net-to-gross facies is comparable to sequence-stratigraphic stacking patterns interpreted for other outcropping lobe deposits (e.g. the progradation–aggradation–retrogradation cycle of Hodgson et al., 2006). However, we choose to not speculate on the sequence-stratigraphic framework or the associated forcing mechanisms for the limited areal exposures of the Point Loma Formation.

The progressive vertical de-amalgamation in Element 4-8 suggests progressive abandonment of the lobe, perhaps via avulsion (Sapardina, 2023) or by allogenic forcing (e.g. Jobe et al., 2017). The mudstone-rich Complex 5 deposits represent dilute turbidity currents in either a distal or lateral fringe location, where the axial facies of the lobe complex was deposited farther upslope or laterally (Figure 13). The depositing currents may also have been sourced from a different feeder system, given the *ca* 50° shift in paleocurrent direction in Complex 5 compared to Complexes 4 and 6 (Figures 2 and 13). While the location of Complex 5 in Figure 13 honours these data, the location of the axis of Complex 5 is purely speculative. No strong evidence of bottom current deposits was found in Complex 5, but given the complexity of forearc slopes, bottom currents could have also played a role in sediment redistribution in Complex 5 (e.g. Fuhrmann et al., 2022; Lee & Ogawa, 1998). The cessation of sand-rich sediment supply to this area may have been influenced by several factors, including allogenic forcing like tectonics (e.g. Blum et al., 2018; Hou et al., 2021), climatic variability (e.g. Hessler et al., 2018), eustasy (e.g. Cornard et al., 2022; Covault et al., 2007; Jobe et al., 2017; Mason et al., 2019) or autogenic sediment routing changes (e.g. Blum et al., 2017; Hamilton et al., 2015; Jobe et al., 2015). While tectonic forcing is favoured in a forearc basin in a geological time period with no large-magnitude eustastic sea-level oscillations, several of these factors may have played a role in the abrupt shift from sandy (Complex 4) to muddy (Complex 5) sediment supply and then back to sandy supply (Complex 6), and we do not have sufficient data to speculate further on the forcing mechanisms.

Complex 6 has a sharp basal contact with the muddy deposits of Complex 5, suggesting an abrupt and rapid re-establishment of sand-rich, amalgamated lobe deposits by the upslope feeder system. Elements 6-1 and 6-2 show upward-increasing amalgamation, indicating a shift from off-axis to axial facies, with an abrupt shift to more-fringe facies in Element 6-3 (Figure 8A). The re-establishment of amalgamated facies in Element 6-4 that is very similar to 6-2 led us to not interpret this as a lobe-complex boundary. Elements 6-5 and 6-6 have abundant soft-sediment deformation (Figure 8B) that resembles that found in Element 4-5, suggestive of a local slope and/or instability (cf. Dennielou et al., 2017). Element 6-7 contains metre-thick beds with scour-and-fill structures interpreted as Froude-supercritical bedform deposits (e.g. Figures 9 and 12) that are common in channel–mouth and channel–lobe transition zones (e.g. Carvajal et al., 2017; Jobe et al., 2017; Lang, Brandes, & Winsemann, 2017; Postma et al., 2021; Tinterri, 2025). The uppermost Element 6-8 again shows evidence of soft-sediment deformation that is consistent with the overall interpreted CLTZ environment.

At the La Jolla locale, the stacking patterns and facies associations are most like the deposits of Complex 6 at Sunset Cliffs, suggesting a similar sub-environment of a proximal and axial channel–lobe transition zone. The La Jolla elements LJ2, LJ4, and especially the LJ6 (Figure 12C,F) are most comparable to Elements 6-2 (Figure 8A) and 6-8 (Figure 9), showing high net-to-gross FA5 deposits with abundant antidunes and other supercritical-flow deposits (e.g. Fig. 4 of Cornard et al., 2025). The intervening La Jolla elements LJ1, LJ3 and LJ5 (Figure 12E) resemble Element 6-3 (Figure 8A) that is composed of FA3, suggesting a more off-axis locale. However, due to significant difference in paleocurrent direction, La Jolla lobe complexes might not directly relate to the deposition of lobe complexes in Sunset Cliffs even though both could be deposited contemporaneously.

8 | CONCLUSIONS

This study identifies two new lobe complexes in the Upper Cretaceous Point Loma Formation exposed at Sunset Cliffs, San Diego, California. Five facies associations are recognised: MTD, mudstone, mud-rich heterolithic, sand-rich heterolithic and amalgamated sandstone, each representing different architectural positions within an idealised lobe element. Complexes 1–3 are not exposed in this locale, and Complex 4 consists of eight lobe elements that progressively develop from mud-rich heterolithic to tabular sandstone to amalgamated sandstone with antidune and cyclic-step deposits, which we interpreted to represent the progradation and/or compensation of lobe elements through time in a channel–lobe transition zone (CLTZ) setting. A progressive abandonment led to deposition of Complex 5 (first described by this study) that consists of thin-bedded mudstone, inferring a large-scale compensational shift in lobe sedimentation or an allogenically driven pause in sandy sedimentation. An abrupt return to sand-rich sedimentation marks the base of Complex 6 (first described by this study) that consists of eight lobe elements that are sand-rich and have slightly less-organised stacking patterns. The dominant facies association in Complex 6 is amalgamated sandstone that has unstable-antidune deposits that are suggestive of a

localised decrease in slope gradient and/or a decrease in confinement that is common in CLTZ environments. Both flow-parallel and flow-perpendicular exposures constrain the 3D geometries of the antidune deposits in Complex 6, helping to better constrain the recognition criteria for these bedforms. The observed facies associations, Froude-supercritical-flow deposits and scour architecture are all common in CLTZ environments, making this outcrop locale a valuable analog to subsurface CLTZ deposits that are targeted as hydrocarbon accumulations or for carbon storage.

ACKNOWLEDGEMENTS

LS was funded by the Indonesian Endowment of Education (LPDP), with additional support from student grants from the Society for Sedimentary Geology (SEPM), International Association of Sedimentologists (IAS) Judith McKenzie Fund and the Bartshe Fund and Lee Billingsley Graduate Fellowship at Colorado School of Mines. We would also like to thank Shaskia Putri and Nursyam Syahrir for field assistance, and Lesli Wood, Dorrik Stow, Jonathan Wilkins, Dessy Sapardina, Rachel Aisner-Williams, Viska Dewi and Marat Ibagarov for their discussion and feedback. Pauline Cornard, an anonymous reviewer, and Associate Editor Matthieu Cartigny are acknowledged for their careful and very useful suggestions to improve the clarity of the manuscript.

DATA AVAILABILITY STATEMENT

The data that support the findings of this study are available from the corresponding author upon reasonable request.

ORCID

Luthfi Saifudin https://orcid.org/0009-0003-0364-1313
Zane Jobe https://orcid.org/0000-0002-7654-4528
Arnoud Slootman https://orcid.org/0000-0001-8719-3041
Piret Plink-Björklund https://orcid.org/0000-0003-1637-2100

REFERENCES

Alexander, J., Bridge, J.S., Cheel, R.J. & Leclair, S.F. (2001) Bedforms and associated sedimentary structures formed under supercritical water flows over aggrading sand beds. *Sedimentology*, 48, 133–152.

Blum, M., Rogers, K., Gleason, J., Najman, Y., Cruz, J. & Fox, L. (2018) Allogenic and autogenic signals in the stratigraphic record of the Deep-Sea Bengal Fan. *Scientific Reports*, 8(1), 7973. https://doi.org/10.1038/s41598-018-25819-5

Blum, M.D., Milliken, K.T., Pecha, M.A., Snedden, J.W., Frederick, B.C. & Galloway, W.E. (2017) Detrital-zircon records of Cenomanian, Paleocene, and Oligocene Gulf of Mexico drainage integration and sediment routing: Implications for scales of basin-floor fans. *Geosphere*, 13(6), 2169–2205.

Bouma, A.H. (1962) *Sedimentology of some flysch deposits: a graphic approach to facies interpretation*. Amsterdam: Elsevier.

Brooks, H.L., Hodgson, D.M., Brunt, R.L., Peakall, J., Hofstra, M. & Flint, S.S. (2018) Deep-water channel-lobe transition zone dynamics Deep-water channel-lobe transition zone dynamics: Processes and depositional architecture, an example from the Karoo Basin, South Africa. http://pubs.geoscienceworld.org/gsa/gsabulletin/article-pdf/130/9-10/1723/4315878/1723.pdf

Brooks, H.L., Ito, M., Zuchuat, V., Peakall, J. & Hodgson, D.M. (2022) Channel-lobe transition zone development in tectonically active settings: Implications for hybrid bed development. *Depositional Record*, 8(2), 829–868. https://doi.org/10.1002/dep2.180

Bull, S., Cartwright, J. & Huuse, M. (2009) A review of kinematic indicators from mass-transport complexes using 3D seismic data. *Marine and Petroleum Geology*, 26(7), 1132–1151.

Cantelli, A., Pirmez, C., Johnson, S. & Parker, G. (2011) Morphodynamic and stratigraphic evolution of self-channelized subaqueous fans emplaced by turbidity currents. *Journal of Sedimentary Research*, 81(3), 233–247. https://doi.org/10.2110/jsr.2011.20

Cantero, M.I., Balachandar, S., Cantelli, A. & Parker, G. (2014) A simplified approach to address turbulence modulation in turbidity currents as a response to slope breaks and loss of lateral confinement. *Environmental Fluid Mechanics*, 14(2), 371–385. https://doi.org/10.1007/s10652-013-9302-7

Cardona, S., Wood, L.J., Dugan, B., Jobe, Z. & Strachan, L.J. (2020) Characterization of the Rapanui mass-transport deposit and the basal shear zone: Mount Messenger Formation, Taranaki Basin, New Zealand. *Sedimentology*, 67(4), 2111–2148.

Carr, M. & Gardner, M.H. (2000) Chapter 20 Portrait of a Basin-Floor Fan for Sandy Deepwater Systems, Permian Lower Brushy Canyon Formation, West Texas. http://pubs.geoscienceworld.org/books/book/chapter-pdf/3841636/9781629812625_ch20.pdf

Cartigny, M.J.B., Ventra, D., Postma, G. & Den Berg, J.H. (2014) Morphodynamics and sedimentary structures of bedforms under supercritical-flow conditions: New insights from flume experiments. *Sedimentology*, 61, 712–748.

Carvajal, C., Paull, C.K., Caress, D.W., Fildani, A., Lundsten, E., Anderson, K., Maier, K.L., McGann, M., Gwiazda, R. & Herguera, J.C. (2017) Unraveling the channel-lobe transition zone with high-resolution AUV bathymetry: Navy Fan, offshore Baja California, Mexico. *Journal of Sedimentary Research*, 87(10), 1049–1059. https://doi.org/10.2110/jsr.2017.58

Cornard, P.H., Moernaut, J., Moore, G.F., Kioka, A., Kopf, A., dos Santos Ferreira, C. & Strasser, M. (2022) Sequence stratigraphic evolution of the Kumano Forearc basin during the last deglaciation: influence of Eustasy and tectonically-controlled shelf morphology on deep-marine sediment dynamics. *Sedimentary Geology*, 430, 106100. https://doi.org/10.1016/j.sedgeo.2022.106100

Cornard, P.H. & Pickering, K.T. (2020) Submarine Topographic Control on Distribution of Supercritical-Flow Deposits in Lobe and Related Environments, Middle Eocene, Jaca Basin, Spanish Pyrenees. *Journal of Sedimentary Research*, 90(9), 1222–1243. https://doi.org/10.2110/jsr.2020.59

Cornard, P.H., Pickering, K.T. & Strasser, M. (2025) Supercritical-flow deposits: a new quantitative tool to characterise deep-marine depositional environments (Oligocene Annot Sandstones, SE

France)? *Terra Nova*, 37(1), 49–56. https://doi.org/10.1111/ter.12746

Covault, J.A., Normark, W.R., Romans, B.W. & Graham, S.A. (2007) Highstand fans in the California borderland: the overlooked deep-water depositional systems. *Geology*, 35(9), 783–786.

Croguennec, C., Ruffine, L., Dennielou, B., Baudin, F., Caprais, J.C., Guyader, V., Bayon, G., Brandily, C., Le Bruchec, J., Bollinger, C. & Germain, Y. (2017) Evidence and age estimation of mass wasting at the distal lobe of The Congo deep-sea fan. *Deep Sea Research, Part II: Topical Studies in Oceanography*, 142, 50–63.

Cullis, S., Colombera, L., Patacci, M. & McCaffrey, W.D. (2018) Hierarchical classifications of the sedimentary architecture of deep-marine depositional systems. *Earth-Science Reviews*, 179, 38–71.

Dennielou, B., Droz, L., Babonneau, N., Jacq, C., Bonnel, C., Picot, M., Le Saout, M., Saout, Y., Bez, M., Savoye, B. & Olu, K. (2017) Morphology, structure, composition and build-up processes of the active channel-mouth lobe complex of the Congo deep-sea fan with inputs from remotely operated underwater vehicle (ROV) multibeam and video surveys. *Deep Sea Research Part II: Topical Studies in Oceanography*, 142, 25–49.

Deptuck, M.E., Piper, D.J.W., Savoye, B. & Gervais, A. (2008) Dimensions and architecture of late Pleistocene submarine lobes off the northern margin of East Corsica. *Sedimentology*, 55(4), 869–898. https://doi.org/10.1111/j.1365-3091.2007.00926.x

Droz, L., Jégou, I., Gillet, H., Dennielou, B., Bez, M., Canals, M., Amblas, D., Lastras, G. & Rabineau, M. (2020) On the termination of deep-sea fan channels: examples from the Rhône Fan (Gulf of Lion, Western Mediterranean Sea). *Geomorphology*, 369, 107368.

Elliott, T. (2000) Megaflute erosion surfaces and the initiation of turbidite channels. *Geology*, 28(2), 119–122.

Englert, R.G., Hubbard, S.M., Cartigny, M.J.B., Clare, M.A., Coutts, D.S., Hage, S., Hughes Clarke, J., Jobe, Z., Lintern, D.G., Stacey, C. & Vendettuoli, D. (2021) Quantifying the three-dimensional stratigraphic expression of cyclic steps by integrating seafloor and deep-water outcrop observations. *Sedimentology*, 68(4), 1465–1501. https://doi.org/10.1111/sed.12772

Fedele, J.J., Hoyal, D.C., Barnaal, Z., Tulenko, J. & Awalt, S. (2016) Bedforms created by gravity flows. In: Budd, D., Hajek, E. & Purkis, S. (Eds.) *Autogenic Dynamics and Self-Organization in Sedimentary Systems*, Vol. 106. Tulsa: SEPM Special Publication, pp. 95–121.

Fielding, C.R. (2006) Upper flow regime sheets, lenses and scour fills: extending the range of architectural elements for fluvial sediment bodies. *Sedimentary Geology*, 190(1–4), 227–240.

Fleming, A. (2010) Stratigraphic architecture of lobe strata in a submarine fan setting, Point Loma Formation, *California* [Master Thesis]. Colorado School of Mines.

Fryer, R.C. & Jobe, Z.R. (2019) Quantification of the bed-scale architecture of submarine depositional environments. *The Depositional Record*, 5(2), 192–211.

Fryer, R.C., Jobe, Z.R., Laugier, F., Pettinga, L.A., Gilbert, J.C., Shumaker, L.E., Smith, J.E. & Sullivan, M. (2021) Submarine lobe deposits of the Point Loma Formation, California: quantifying event-bed architecture and lateral heterogeneity. *The Depositional Record*, 7(3), 374–391. https://doi.org/10.1002/dep2.156

Fuhrmann, A., Kane, I.A., Schomacker, E., Clare, M.A. & Pontén, A. (2022) Bottom current modification of turbidite lobe complexes. *Frontiers in Earth Science*, 9, 752066.

Girty, G.H. (1987) Sandstone provenance, Point Loma Formation, San Diego, California: evidence for Uplift of the Peninsular Ranges during The Laramide Orogeny. *Journal of Sedimentary Petrology*, 57(5), 839–844.

Hage, S., Cartigny, M.J.B., Clare, M.A., Sumner, E.J., Vendettuoli, D., Hughes Clarke, J.E., Hubbard, S., Talling, P.J., Lintern, D.G., Stacey, C.D., Englert, R.G., Vardy, M.E., Hunt, J.E., Yokokawa, M., Parsons, D.R., Hizzett, J.L., Azpiroz-Zabala, M. & Vellinga, A.J. (2018) How to recognize crescentic bedforms formed by supercritical turbidity currents in the rock record: insights from active submarine channels. *Geology*, 46, 563–566.

Hage, S., Galy, V.V., Cartigny, M.J.B., Acikalin, S., Clare, M.A., Gröcke, D.R., Hilton, R.G., Hunt, J.E., Lintern, D.G., Mcghee, C.A., Parsons, D.R., Stacey, C.D., Sumner, E.J. & Talling, P.J. (2020) Efficient preservation of young terrestrial organic carbon in sandy turbidity-current deposits. *Geology*, 48(9), 882–887. https://doi.org/10.1130/G47320.1

Hamilton, P.B., Strom, K.B. & Hoyal, D.C. (2015) Hydraulic and sediment transport properties of autogenic avulsion cycles on submarine fans with supercritical distributaries. *Journal of Geophysical Research: Earth Surface*, 120(7), 1369–1389.

Hand, B.M. (1974) Supercritical flow in density currents. *Journal of Sedimentary Petrology*, 44, 637–648.

Haughton, P., Davis, C., McCaffrey, W. & Barker, S. (2009) Hybrid sediment gravity flow deposits – Classification, origin and significance. *Marine and Petroleum Geology*, 26(10), 1900–1918. https://doi.org/10.1016/J.MARPETGEO.2009.02.012

Hessler, A.M., Covault, J.A., Stockli, D.F. & Fildani, A. (2018) Late Cenozoic cooling favored glacial over tectonic controls on sediment supply to the western Gulf of Mexico. *Geology*, 46(11), 995–998.

Hessler, A.M. & Fildani, A. (2019) Deep-sea fans: tapping into Earth's changing landscapes. *Journal of Sedimentary Research*, 8(11), 1171–1179. https://doi.org/10.2110/jsr.2019.64

Hickson, T.A. & Lowe, D.R. (2002) Facies architecture of a submarine fan channel–levee complex: the Juniper Ridge Conglomerate, Coalinga, California. *Sedimentology*, 49(2), 335–362.

Hodgson, D.M., Flint, S.S., Hodgetts, D., Drinkwater, N.J., Johannessen, E.P. & Luthi, S.M. (2006) Stratigraphic evolution of fine-grained submarine fan systems, Tanqua depocenter, Karoo Basin, South Africa. *Journal of Sedimentary Research*, 76(1), 20–40.

Hofstra, M., Hodgson, D.M., Peakall, J. & Flint, S.S. (2015) Giant scour-fills in ancient channel-lobe transition zones: formative processes and depositional architecture. *Sedimentary Geology*, 329, 98–114. https://doi.org/10.1016/j.sedgeo.2015.09.004

Hofstra, M., Peakall, J., Hodgson, D.M. & Stevenson, C.J. (2018) Architecture and morphodynamics of subcritical sediment waves in an ancient channel–lobe transition zone. *Sedimentology*, 65(7), 2339–2367.

Hou, P., Wood, L.J. & Jobe, Z.R. (2021) Tectonic–sedimentary interplay of a confined deepwater system in a foreland basin setting: the Pennsylvanian lower Atoka Formation, Ouachita Mountains, USA. *Journal of Sedimentary Research*, 91(7), 683–709.

Hughes Clarke, J.H. (2016) First wide-angle view of channelized turbidity currents links migrating cyclic steps to flow characteristics. *Nature Communications*, 7, 11896.

Ito, M. (2008) Downfan transformation from turbidity currents to debris flows at a channel-to-lobe transitional zone: The lower Pleistocene Otadai Formation, Boso Peninsula, Japan. *Journal of Sedimentary Research*, 78(10), 668–682. https://doi.org/10.2110/jsr.2008.076

Jaikla, C. (2021) Resolving sedimentology, stratigraphic architecture and evolution of deep-water systems in two structurally complex areas: the upper cretaceous Pigeon Point Formation, California, and the Oligocene Molasse Basin, Austria, unpublished thesis from Stanford University

Jiang, H. & Lee, C.T.A. (2017) Coupled magmatism–erosion in continental arcs: reconstructing the history of the Cretaceous Peninsular Ranges batholith, southern California through detrital hornblende barometry in forearc sediments. *Earth and Planetary Science Letters*, 472, 69–81. https://doi.org/10.1016/J.EPSL.2017.05.009

Jobe, Z.R., Bernhardt, A. & Lowe, D.R. (2010) Facies and architectural asymmetry in a conglomerate-rich submarine channel fill, Cerro Toro Formation, Sierra del Toro, Magallanes Basin, Chile. *Journal of Sedimentary Research*, 80(12), 1085–1108.

Jobe, Z.R., Howes, N., Martin, J., Meyer, R., Coutts, D., Hou, P., Stright, L. & Laugier, F. (2021) Sedimentary graphic logs: a template for description and a toolkit for digitalization. *The Sedimentary Record*, 19(3), 15–29.

Jobe, Z.R., Lowe, D.R. & Morris, W.R. (2012) Climbing-ripple successions in turbidite systems: depositional environments, sedimentation rates and accumulation times. *Sedimentology*, 59, 867–898. https://doi.org/10.1111/j.1365-3091.2011.01283.x

Jobe, Z.R., Sylvester, Z., Howes, N., Pirmez, C., Parker, A., Cantelli, A., Smith, R., Wolinsky, M.A., O'Byrne, C., Slowey, N. & Prather, B. (2017) High-resolution, millennial-scale patterns of bed compensation on a sand-rich intraslope submarine fan, western Niger Delta slope. *Bulletin*, 129(1–2), 23–37.

Jobe, Z.R., Sylvester, Z., Parker, A.O., Howes, N., Slowey, N. & Pirmez, C. (2015) Rapid adjustment of submarine channel architecture to changes in sediment supply. *Journal of Sedimentary Research*, 85(6), 729–753.

Kane, I.A. & Clare, M.A. (2019) Dispersion, accumulation, and the ultimate fate of microplastics in deep-marine environments: a review and future directions. *Frontiers in Earth Science*, 7, 80. https://doi.org/10.3389/feart.2019.00080

Kane, I.A., McCaffrey, W.D. & Martinsen, O.J. (2009) Allogenic vs. autogenic controls on megaflute formation. *Journal of Sedimentary Research*, 79(9–10), 643–651. https://doi.org/10.2110/jsr.2009.072

Kennedy, J.F. (1963) The mechanics of dunes and antidunes in erodible-bed channels. *Journal of Fluid Mechanics*, 16, 521–544.

Kennedy, M.P. (1975) *Geology of the San Diego metropolitan area, California*. California Divisions of Mines and Geology, Bulletin 200A (accessed from the USGS National Geologic Map Database).

Kennedy, M.P. & Moore, G.W. (1971) Stratigraphic Relations of Upper Cretaceous and Eocene Formations, Son Diego Coastal Area, California. *American Association of Petroleum Geologists Bulletin*, 55(5), 709–722.

Kenyon, N.H., Millington, J., Droz, L. & Ivanov, M.K. (1995) Scour holes in a channel-lobe transition zone on the Rhöne Cone. In: PIckering, K.T., Hiscott, R.N., Kenyon, N.H., RIchi Luchi, F. & Smith, R.D.A. (Eds.) *Atlas of deep water environments*. London: Chapman and Hall, pp. 333.

Komar, P.D. (1971) The mechanics of sand transport on beaches. *Journal of Geophysical Research*, 76(3), 713–721. https://doi.org/10.1029/jc076i003p00713

Kus, K.B., Jobe, Z.R., Laugier, F., Walker, W. & Sullivan, M. (2022) Quantifying the lateral heterogeneity of distal submarine lobe deposits, Point Loma Formation, California: implications for subsurface lateral facies prediction. *The Depositional Record*, 8(2), 472–501. https://doi.org/10.1002/dep2.169

Lang, J., Brandes, C. & Winsemann, J. (2017) Erosion and deposition by supercritical density flows during channel avulsion and backfilling: field examples from coarse-grained deepwater channel-levée complexes (Sandino Forearc Basin, Southern Central America). *Sedimentary Geology*, 349, 79–102. https://doi.org/10.1016/j.sedgeo.2017.01.002

Lang, J., Sievers, J., Loewer, M., Igel, J. & Winsemann, J. (2017) 3D architecture of cyclic-step and antidune deposits in glacigenic subaqueous fan and delta settings: Integrating outcrop and ground-penetrating radar data. *Sedimentary Geology*, 362, 83–100. https://doi.org/10.1016/J.SEDGEO.2017.10.011

Lee, I. & Ogawa, Y. (1998) Bottom-current deposits in the Miocene–Pliocene Misaki Formation, Izu forearc area, Japan. *Island Arc*, 7(3), 315–329.

Lobato, G., Postma, G., Lintern, D.G., Jacinto, R.S. & Cartigny, M.J. (2025) Decadal architecture and morphodynamics of modern, river-fed turbidite systems: Bute Inlet and Congo Fan. *Journal of Sedimentary Research*, 95(1), 104–132.

Lowe, D.R. (1975) Water escape structures in coarse-grained sediments. *Sedimentology*, 22, 157–204. https://doi.org/10.1111/j.1365-3091.1975.tb00290.x

Lowe, D.R. (1982) Sediment gravity flows: II. Depositional models with special reference to the deposits of high-density turbidity currents. http://pubs.geoscienceworld.org/sepm/jsedres/article-pdf/52/1/279/2808789/279.pdf

Macdonald, H.A., Wynn, R.B., Huvenne, V.A.I., Peakall, J., Masson, D.G., Weaver, P.P.E. & McPhail, S.D. (2011) New insights into the morphology, fill, and remarkable longevity (>0.2 m.y.) Of modern deep-water erosional scours along the northeast Atlantic margin. *Geosphere*, 7(4), 845–867. https://doi.org/10.1130/GES00611.1

Mansor, H.E. & Amir Hassan, M.H. (2021) Facies and bed type characteristics of channel-lobe transition deposits from the Oligocene-Miocene Tajau Sandstone Member, Kudat Formation, Sabah, Malaysia. *Geological Journal*, 56(11), 5642–5672. https://doi.org/10.1002/gj.4263

Mason, C.C., Romans, B.W., Stockli, D.F., Mapes, R.W. & Fildani, A. (2019) Detrital zircons reveal sea-level and hydroclimate controls on Amazon River to deep-sea fan sediment transfer. *Geology*, 47(6), 563–567.

McGlown, A. (2015) Transitional flow deposits in submarine lobe strata: the Cretaceous Point Loma Formation, San Diego, California. Thesis, University of Texas at Austin.

Mutti, E. & Normark, W. (1987) Comparing examples of modern and ancient turbidite systems: problems and concepts. In: Leggett, J.K. & Zuffa, G.G. (Eds.) *Marine clastic sedimentology*. Dordrecht: Springer. https://doi.org/10.1007/978-94-009-3241-8_1

Nardin, T.R., Hein, F.J., Gorsline, D.S. & Edwards, B.D. (1979) A review of mass movement processes, sediment and acoustic characteristics, and contrasts in slope and base-of-slope systems versus canyon- fan- basin floor systems [SEPM Special

Publication]. *Geology of Continental Slopes*, 27, 61–73. https://doi.org/10.2110/pec.79.27.0061

Nilsen, T.H. & Abbott, P.L. (1981) Paleogeography and sedimentology of upper Cretaceous turbidites, San Diego, California. *AAPG Bulletin*, 65(7), 1256–1284.

Normandeau, A., MacKillop, K., Richards, C., Philibert, G., Montero-Serrano, J.C., Macquarrie, M. & Bennett, R. (2025) Processes and products of turbidity currents and submarine landslides in a glacierized fjord (Southwind Fjord, Baffin Island). *Geochemistry, Geophysics, Geosystems*, 26(4), e2024GC011710.

Normark, W., Piper, D. & Hess, G. (1979) Distributary channels, sand lobes, and mesotopography of Navy Submarine Fan, California Borderland, with applications to ancient fan sediments. *Sedimentology*, 26(6), 749–774. https://doi.org/10.1111/j.1365-3091.1979.tb00971.x

Ono, K. & Plink-Björklund, P. (2018) Froude supercritical flow bedforms in deepwater slope channels? Field examples in conglomerates, sandstones and fine-grained deposits. *Sedimentology*, 65(3), 639–669. https://doi.org/10.1111/sed.12396

Pemberton, E.A.L., Hubbard, S.M., Fildani, A., Romans, B. & Stright, L. (2016) The stratigraphic expression of decreasing confinement along a deep-water sediment routing system: outcrop example from southern Chile. *Geosphere*, 12(1), 114–134. https://doi.org/10.1130/GES01233.1

Peterson, G. & Nordstorm, C. (1970) Sub-La Jolla Unconformity in Vicinity of San Diego, California. *American Association of Petroleum Geologists Bulletin*, 54(2), 265–274. http://pubs.geoscienceworld.org/aapgbull/article-pdf/54/2/265/4400088/aapg_1970_0054_0002_0265.pdf

Pettinga, L., Jobe, Z., Shumaker, L. & Howes, N. (2018) Morphometric scaling relationships in submarine channel-lobe systems. *Geology*, 46(9), 819–822. https://doi.org/10.1130/G45142.1

Pickering, K.T., Corregidor, J. & Clark, J.D. (2015) Architecture and stacking patterns of lower-slope and proximal basin-floor channelised submarine fans, Middle Eocene Ainsa System, Spanish Pyrenees: an integrated outcrop–subsurface study. *Earth-Science Reviews*, 144, 47–81.

Picot, M., Droz, L., Marsset, T., Dennielou, B. & Bez, M. (2016) Controls on turbidite sedimentation: insights from a quantitative approach of submarine channel and lobe architecture (Late Quaternary Congo Fan). *Marine and Petroleum Geology*, 72, 423–446.

Piper, D.J.W., Pirmez, C., Manley, P.L., Long, D., Flood, R.D., Normark, W.R. & Showers, W. (1997) Mass-transport deposits of the Amazon Fan. In: *Proceedings-ocean drilling program scientific results*. College Station: National Science Foundation, pp. 109–146.

Pohl, F., Eggenhuisen J., deLeeuw J., Cartigny M., Brooks H. & Spychala Y., (2022) Reconstructing sedimentary processes in a Permian channel–lobe transition zone: an outcrop study in the Karoo Basin, South Africa. *Geological Magazine*, 160(1), 107–126. https://doi.org/10.1017/S0016756822000693

Pohl, F., Eggenhuisen, J.T., Cartigny, M.J.B., Tilston, M.C., De Leeuw, J. & Hermidas, N. (2020) The influence of a slope break on turbidite deposits: an experimental investigation. *Marine Geology*, 424, 106160.

Postma, G., Cartigny, M. & Kleverlaan, K. (2009) Structureless, coarse-tail graded Bouma Ta formed by internal hydraulic jump of the turbidity current? *Sedimentary Geology*, 219(1–4), 1–6.

Postma, G. & Cartigny, M.J.B. (2014) Supercritical and subcritical turbidity currents and their deposits—a synthesis. *Geology*, 42(11), 987–990. https://doi.org/10.1130/G35957.1

Postma, G. & Kleverlaan, K. (2018) Supercritical flows and their control on the architecture and facies of small-radius sand-rich fan lobes. *Sedimentary Geology*, 364, 53–70. https://doi.org/10.1016/j.sedgeo.2017.11.015

Postma, G., Lang, J., Hoyal, D.C., Fedele, J.J., Demko, T., Abreu, V. & Pederson, K.H. (2021) Reconstruction of bedform dynamics controlled by supercritical flow in the channel–lobe transition zone of a deep-water delta (Sant Llorenç del Munt, north-east Spain, Eocene). *Sedimentology*, 68(4), 1674–1697. https://doi.org/10.1111/sed.12735

Prélat, A. & Hodgson, D.M. (2013) The full range of turbidite bed thickness patterns in submarine lobes: Controls and implications. *Journal of the Geological Society*, 170(1), 209–214. https://doi.org/10.1144/jgs2012-056

Prélat, A., Hodgson, D.M. & Flint, S.S. (2009) Evolution, architecture and hierarchy of distributary deep-water deposits: a high-resolution outcrop investigation from the Permian Karoo Basin, South Africa. *Sedimentology*, 56(7), 2132–2154. https://doi.org/10.1111/j.1365-3091.2009.01073.x

Pyles, D.R., Fleming, A.E.P. & Anderson, D.S. (2019) Hierarchical organization and spatial variations of lobes in distributive submarine fans: Outcrop study of the Point Loma Formation, California, USA. *SEPM Special Publication*, 110, 135–157. https://doi.org/10.2110/sepmsp.110.09

Sapardina, D.W. (2023) *The Role of Froude Supercritical Flow in Active Margin Basin-Flow Fans* [Dissertation]. Colorado School of Mines.

Sequeiros, O.E. (2012) Estimating turbidity current conditions from channel morphology: a Froude number approach. *Journal of Geophysical Research-Oceans*, 117(C4).

Sharman, G.R., Graham, S.A., Grove, M., Kimbrough, D.L. & Wright, J.E. (2015) Detrital zircon provenance of the Late Cretaceous-Eocene California forearc: influence of Laramide low-angle subduction on sediment dispersal and paleogeography. *Bulletin of the Geological Society of America*, 127(1–2), 38–60. https://doi.org/10.1130/B31065.1

Simabrata, H., Jobe, Z.R., Wood, L.J., Cardona, S. & Hou, P. (2025) Characterization, prediction and implications of compartments in a mixed carbonate–siliciclastic mass-transport complex: the Cutoff Formation, Permian Basin, Texas. *Sedimentology*, 72(4), 1102–1131. https://doi.org/10.1111/sed.13269

Simons, D.B. & Richardson, E.V. (1961) Forms of bed roughness in alluvial channels. *Journal of Hydraulic Engineering*, 86, 73–99.

Sliter, W.V. (1984) Cretaceous foraminifers from La Jolla, California. In: *Upper Cretaceous depositional systems*. Southern California: Pacific Section – SEPM, pp. 35–36.

Slootman, A. & Cartigny, M.J.B. (2020) Cyclic steps: Review and aggradation-based classification. *Earth-Science Reviews*, 201, 102949. https://doi.org/10.1016/J.EARSCIREV.2019.102949

Slootman, A., De Boer, P.L., Cartigny, M.J., Samankassou, E. & Moscariello, A. (2019) Evolution of a carbonate delta generated by gateway-funnelling of episodic currents. *Sedimentology*, 66(4), 1302–1340.

Slootman, A., Vellinga, A.J., Moscariello, A. & Cartigny, M.J.B. (2021) The depositional signature of high-aggradation chute-and-pool

bedforms: the build-and-fill structure. *Sedimentology*, 68(4), 1640–1673. https://doi.org/10.1111/sed.12843

Spychala, Y.T., Hodgson, D.M., Prélat, A., Kane, I.A., Flint, S.S. & Mountney, N.P. (2017) Frontal and lateral submarine lobe fringes: comparing sedimentary facies, architecture and flow processes. *Journal of Sedimentary Research*, 87(1), 75–96. https://doi.org/10.2110/jsr.2017.2

Stammer, J.G. (2014) *Hydrodynamic Fractionation of Minerals and Textures in Submarine Fans: Quantitative Analysis from outcrop, Experimental, and Subsurfae Studies* [Dissertation]. Colorado School of Mines.

Stow, D.A.V., Huc, A.Y. & Bertrand, P. (2001) Depositional processes of black shales in deep water. *Marine and Petroleum Geology*, 18(4), 491–498.

Symons, W.O., Sumner, E.J., Talling, P.J., Cartigny, M.J. & Clare, M.A. (2016) Large-scale sediment waves and scours on the modern seafloor and their implications for the prevalence of supercritical flows. *Marine Geology*, 371, 130–148.

Talling, P.J., Baker, M.L., Pope, E.L., Ruffell, S.C., Silva Jacinto, R., Heijnen, M.S., Hage, S., Simmons, S.M., Hasenhündl, M., Heerema, C.J., McGhee, C., Apprioual, R., Ferrant, A., B Cartigny, M.J., Parsons, D.R., Clare, M.A., Tshimanga, R.M., Trigg, M.A., Cula, C.A., Cula, C.A., Faria, R., Gaillot, A., Bola, G., Wallance, D., Griffiths, A., Nunny, R., Urlaub, M., Peirce, C., Burnett, R., Neasham, J. & Hilton, R.J. (2022) Longest sediment flows yet measured show how major rivers connect efficiently to deep sea. *Nature Communications*, 13, 4193.

Talling, P.J., Hage, S., Baker, M.L., Bianchi, T.S., Hilton, R.G. & Maier, K.L. (2024) The global turbidity current pump and its implications for organic carbon cycling. *Annual Review of Marine Science*, 16(1), 105–133.

Talling, P.J., Wynn, R.B., Schmmidt, D.N., Rixon, R., Sumner, E. & Amy, L. (2010) How did thin submarine debris flows carry boulder-sized intraclasts for remarkable distances across low gradients to the far reaches of the Mississippi Fan? *Journal of Sedimentary Research*, 80(10), 829–851.

Tinterri, R. (2025) A new turbidite facies-tract scheme including supercritical and transitional sand–mud flows: an outcrop perspective from Mediterranean-type foreland basins. *Journal of Sedimentary Research*, 95(2), 239–272.

Twichell, D.C., Schwab, W.C., Nelson, C.H., Kenyon, N.H. & Lee, H.J. (1992) Characteristics of a sandy depositional lobe on the outer Mississippi fan from SeaMARC IA sidescan sonar images. *Geology*, 20(8), 689–692.

Van Der Merwe, W.C., Hodgson, D.M. & Flint, S.S. (2009) Widespread syn-sedimentary deformation on a muddy deep-water basin-floor: the Vischkuil Formation (Permian), Karoo Basin, South Africa. *Basin Research*, 21(4), 389–406.

Walker, R.G. (1965) The origin and significance of the internal sedimentary structures of turbidites. *Proceedings of the Yorkshire Geological Society*, 35(1), 1–32.

Wilkin, J., Cuthbertson, A., Dawson, S., Stow, D., Stephen, K., Nicholson, U. & Penna, N. (2023) The response of high density turbidity currents and their deposits to an abrupt channel termination at a slope break: Implications for channel–lobe transition zones. *Sedimentology*, 70(4), 1164–1194.

Wood, L., Moscardelli, L., Dunlap, D. & Cardona, S. (2015) Healing-Phase, Top-Trapped Fills associated with Mass Transport Complexes: Controls on Turbidite deposition in Chaotic Margin Settings. AAPG Datapages.

Wynn, R.B., Kenyon, N.H., Masson, D.G., Stow, D.A.V. & Weaver, P.P.E. (2002) Characterization and Recognition of Deep-water Channel-lobe Transition Zones. *AAPG Bulletin*, 86(8), 1441–1462.

Yeo, R.K. (1984) Field guide-miocene and cretaceous depositional enviroments of Northwestern Baja California, Mexico. In: Minch, J.A. & Ashby, J.R. (Eds.) *Miocene and cretaceous depositional environments, Northwestern Baja California, Mexico*, Vol. 54. Bakersfield, CA: Pacific Section A.A.P.G., pp. 1–18.

Yokokawa, M., Okuno, K., Nakamura, A., Muto, T., Miyata, Y., Naruse, H. & Parker, G. (2009) Aggradational cyclic steps: sedimentary structures found in flume experiments. International Association for Hydro-Environment Engineering and Research, 33rd Congress, Proceedings, 5547–5554.

How to cite this article: Saifudin, L., Jobe, Z., Slootman, A., Carr, M. & Plink-Björklund, P. (2026) Supercritical-flow structures in a Cretaceous submarine channel–lobe transition zone, Point Loma Formation, California. *The Depositional Record*, 12, e70070. Available from: https://doi.org/10.1002/dep2.70070